Prismatic axis, differential-drive robotic kiwifruit harvester for reduced cycle time

THE UNIVERSITY OF
WAIKATO
Te Whare Wānanga o Waikato

A thesis submitted
in fulfilment
of the requirements
for the degree of

Master of Engineering

At

The University of Waikato

Josh Barnett

2018

Abstract

The New Zealand kiwifruit industry is currently worth over NZD 2 billion in annual sales revenue, this is forecast to double within the next 5-10 years due to a significant increase in production volume. The industry is already experiencing a prevalent shortage of labour which is indicative of a global trend. The objective for this study was to define important metrics for the robotic harvesting of kiwifruit and to propose a hardware configuration which could improve on the current kiwifruit harvesting module (KHM) developed by the Multipurpose Orchard Robotics (MOR) project. The research scope was focused to establishing whether a prismatic axis kinematic structure was more effective than a rotational axis kinematic structure for the multiple-robot harvesting of kiwifruit. KPI's (key performance indicators) were defined as evaluation and design measures - these included fruit damage, harvestability and nominal harvest cycle time. An equation specific to the KHM was derived for the latter which included measures of fruit per harvesting phase, time between fruit and a proposed work distribution constant W_D. A prismatic axis, linear rail constrained, kiwifruit harvesting robot (LHR) with two robot-arms was developed, built and tested. It was found to be exponentially beneficial to locate mass proximal to the X axis carriage centers which is achieved with a differential-drive of the YZ axis'. The prismatic axis kinematic structure of the LHR allowed for an 88% greater work distribution constant W_D, a 40% greater harvestable taskspace volume V_h and 2.5 times greater overall workspace efficiency when compared to the KHM. The nominal harvest cycle time was identical for both of these systems. However, the LHR and the developed 'x-rank' registery algorithm were capable of maintaining W_D value despite a two-fold increase in robot-arm density. Therefore, in non-collision scenarios the LHR can operate with four robot-arms without compromising performance. In this scenario where both systems have four robot-arms, the LHR had a 44% reduction in harvest cycle time. Further study would need to be done into manipulability measures, scheduling methods and the effects on work distribution to establish whether a prismatic axis structure remains favourable if an orientation structure is implemented for end-effector dexterity.

Acknowledgements

Firstly, the author would like to acknowledge Professor Mike Duke and The University of Waikato for funding and supporting this research as part of the wider Multi-Purpose Orchard Robotics project. The author would also like to acknowledge Robotics Plus Ltd for providing a development space and research opportunity.

There are several people who helped to make this project happen. Gordon Neshaussen helped with procurement for the entire project from start to finish. Dr Mark Jones and Matthew Seabright were often willing to share thoughts around research, control and software development - they have certainly had a positive influence on this project. Supervisor Dr Chi Kit Au has helped with thesis layout and time management. Canaan Ting made fake kiwifruit for lab testing which was used for end-effector development, he also helped with video and data capture. Michael Redstall also contributed to the project with capturing data and helping with operation. Thanks for your help everyone.

I'd also like to thank my partner Charnade who has been patient and understanding with all the long days and time appart. Also to my family who have been supportive of my journey through University study.

Declarations

I declare that this thesis has been composed independently. Except where stated otherwise by reference or acknowledgment, the work presented is entirely my own. This includes:

- The mechanical design of a prismatic axis kiwifruit harvesting robot with two differential-drive cooperative manipulators. Starting from the idea through to concept and functional prototype
- The electrical and systems design for the robot
- The mechanical design of a novel, fruit-picking end-effector and kiwifruit force detachment jig
- All mechanical and electrical assembly
- All software used on the robot, including:
  - All front-end controller code for motion, homing etc
  - All back-end Python development, including:
    - General programming for robot operation
    - Scheduling algorithms for register allocation
    - Motion optimization program for stepper motors

Signed: _____

Josh Barnett

28/07/2018

Contents

List of Figures

List of Tables

Chapter 1

Introduction

1.1 Background

In 2025, the global precision-agriculture market is predicted to be worth in excess of USD 10 billion, with a compound annual growth of 14.2% [7]. There are several factors causing this growth; the principal drivers being population increase and labour shortage. The United Nations is anticipating a global population increase to 9.8 billion people by 2050 [8], however in many developed countries the working-age demographic is declining. Furthermore, 68% of the worlds population is projected to be urban-based by 2050 [9]. In short, there will be more mouths to feed and less people working to feed them [10]. Also consider environmental pressures and economic returns; there are clear incentives for the development of technologies capable of automating and optimizing agriculture.

Traditionally, PA (precision-agriculture) has been segmented into hardware, software and services. Despite significant growth forecast in the software component of PA, the hardware component was responsible for 72% of the USD 3.06 billion PA market in 2016. Since the industrial revolution, hardware has been used within agriculture in the form of machinery and mechanized tools; causing a significant rise in productivity [11]. That being said, there are limitations to the range of work that a typical 'non-intelligent', human-operated machine can complete. Many agricultural tasks inherit, to some degree, complexity from the natural world and will often require dexterity, delicacy and accuracy. Going forward, agricultural tasks will also require autonomy. The emergent field of agricultural robotics - a subset of PA, aims to address these task requirements with 'intelligent' machines; taking sensory information from the robots' environment and processing this information to produce informed action [12]. The premise is not new - agricultural robots were

being proposed in the early 1980's, and in 2018 the field is a still in its relative infancy. Barriers to progression have been multidisciplinary [13], but with an ever-growing incentive for development - advancements in supporting technologies are becoming ever-more frequent.

The kiwifruit industry in New Zealand has been in a state of recovery in recent years after an invasive pathogen was found present in crops throughout the country during late 2010 [14]. In 2018, the industry is now well recovered with annual sales revenue in excess of NZD 2 billion. All kiwifruit produced in New Zealand are currently marketed under the Zespri label; a grower owned company who is responsible for selling 30% of the worlds kiwifruit by volume. By amalgamating the export of kiwifruit from New Zealand, Zespri has been able to centralize supply chain management and assure a premium standard of exported fruit. This premium image has been the cornerstone of the Zespri brand strategy. Zespri also allocate up to 1.5% of its NZ profits back into an integrated innovation program where they develop new cultivars of kiwifruit, such as their popular gold variety 'SunGold'. Zespri's ambitious growth goal is to increase annual sales revenue to NZD 4.5 billion by 2025 [15]. To achieve this, Zespri are planning to dramatically increase the production volume of their higher-value golden strains. Their plan is to licence an additional 750 hectares of SunGold kiwifruit orchards per year over the next 5 years, albeit maintaining their green kiwifruit production volume. It is forecast that by 2022, those additional SunGold orchards will have been responsible for doubling the volume of SunGold fruit from 45 million trays to over 88 million trays. Zespri and the New Zealand Kiwifruit industry will likely experience some challenges throughout this growth period, though one of those challenges is already prevalent today - a shortage of labor. As of May 2018, the New Zealand government has declared that the industry is short by 1200 staff with another 14000 needed by 2030. Kiwifruit picking and packing are seasonal, physical and repetitive jobs that New Zealanders are not generally interested in applying for. Going forward, a strategy will likely need to be developed for incentivizing labor to secure one of New Zealand's most lucrative exports.

Some forward-thinking New Zealanders have been devising an alternative solution to the kiwifruit industry's labour shortage. The Multipurpose Orchard Robotics project, led by Prof Bruce Mac Donald, is a collaborative effort between the University of Waikato, University of Auckland, Plant and Food Research and commercial partner Robotics Plus. The project goal is to develop autonomous robotic harvesting and pollination systems - not only for kiwifruit but also for apples (another industry short of labour in New Zealand). The project aims to expand

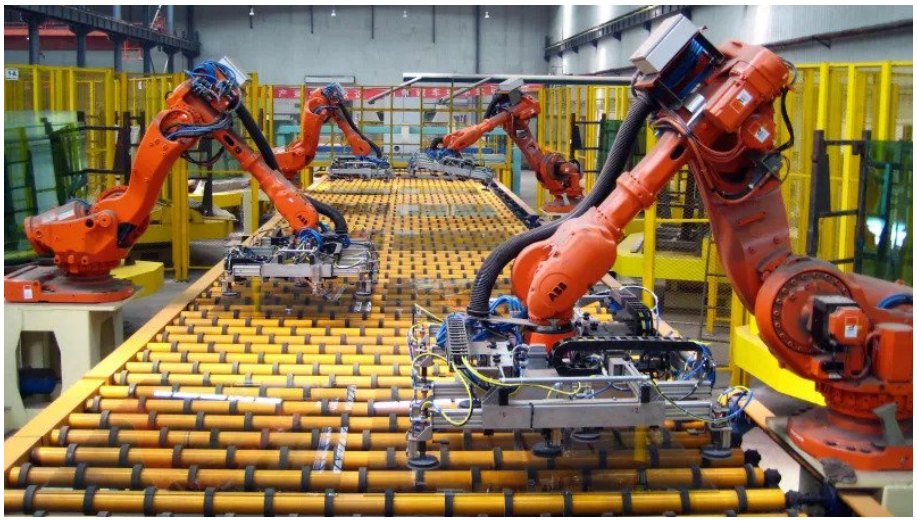

Figure 1.1: Industrial 6 axis robots working on a production line

on work done by Massey University and Dr Alistair Scarfe, who presented a prototype kiwifruit harvesting robot as part of his PhD. In the future, outcomes from this project will likely facilitate growth within the New Zealand horticultural industry, helping businesses such as Zespri to sustain their visionary growth in kiwifruit exports.

1.2 Research objective

An industrial robot typically consists of a manipulator and an end-effector. The manipulator and end-effector relationship is analogous to the human arm and hand; the manipulator provides a means of moving the end-effector through space to programmable task locations and the end-effector produces a task-specific action i.e. grabbing, cutting etc. The industry standard manipulator is the six rotational-axis robotic arm, as shown in Fig. 1.1 using a vacuum 'pick and place' end-effector. Six axis' provide six DOF's (degrees of freedom) which accommodates positioning in any 3D orientation within the robots work-space. However, a standalone six axis robot-arm is not necessarily optimum for every task. Without the need for any rotational manipulation of the end-effector, a three-axis arm provides all DOF's necessary for 3D positioning. Scarfe et al. [16] used this approach, developing a three-axis planar articulated (RRR) arm for picking kiwifruit on the Autonomous kiwifruit harvester (AKH). The AKH design was continued into later development through the MOR project where an array of these arms were used to pick fruit whilst mounted to an autonomous platform (AMMP), see figure 1.2. However, there are speculative avenues for improvement within this configuration, such as:

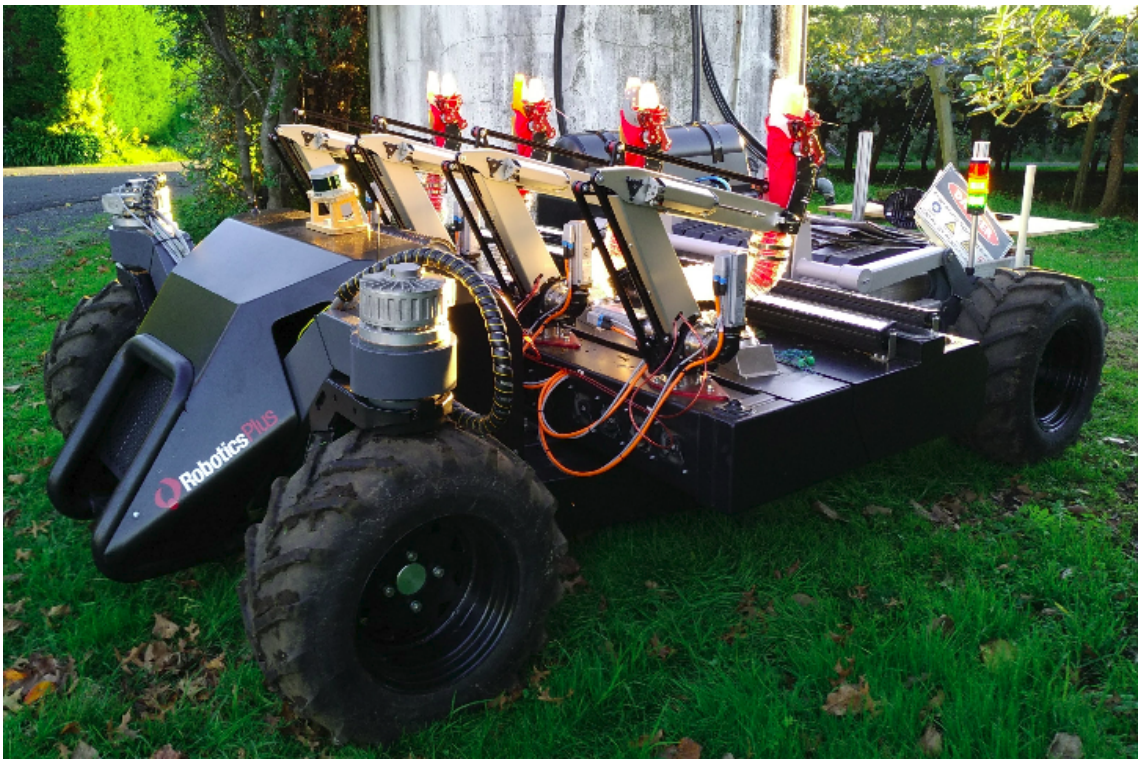

Figure 1.2: Kiwifruit picking robot, New Zealand

- Distribution of work between robot-arms
- The reachable space of the robot-arms in relation to the kiwifruit orchard canopy
- The harvesting efficiency of the end-effector
- Scalability of the configuration

The objective of this research was to define important metrics for the robotic harvesting of kiwifruit and to propose a hardware configuration which could improve on the current multiple RRR robot-arm system. An initial hypothesis is that a prismatic axis robot may demonstrate improvement in multiple robot-arm cooperation by utilizing a shared work space along a common X-axis. It is hoped that the research in hardware configuration as part of this study will progress the field of kiwifruit harvesting automation toward a commercially viable system for allieviating current labour shortage. The following chapter will review relevant topics to formulate a more definitive research goal.

Chapter 2

Review

The strategy for this review is to establish a knowledge base from relevant fields of research to guide the direction of further research and development. Inline with the objective - robotic harvesting systems will be reviewed with a focus on hardware, initially from a generic perspective and then specific to the harvesting of kiwifruit. To start the chapter, robot manipulation measures will be reviewed to the development.

2.1 Performance of a manipulator

The taskspace is a set of positions in space that the end-effector must reach to complete a given task. The workspace on the other hand, is the total volume reachable by the end-effector as the manipulator excutes all possible motions [17]. In applications dependent on end-effector orientation, a measure of dexterity is also of importance within a workspace. The dexetrous workspace is a subset of total workspace that can be approached from all orientations [18]. Manipulators are typically comprised of a regional structure and an orientation structure [19]. Whereby the regional structure provides the spatial component of a workspace and the orientation structure provides some variable orientation of the end-effector. The basic objective for designing a manipulator should be to ensure that the taskspace is some subset of the manipulators workspace and that the dexterity of the manipulator allows for the required orientation of the end-effector at those task positions. This section aims to extend on this by reviewing quantiative evaluation methods of single and multi-robot systems. There have been several performance indices developed for measuring the efficacy of serial and parallel chain manipulators [1]. Quantitative measures such as performance indices provide an explicit, objective basis on which to design and evaluate. These measures should not replace intuition and experience in the design and evaluation process, but act as tools to facilitate an analytical nar-

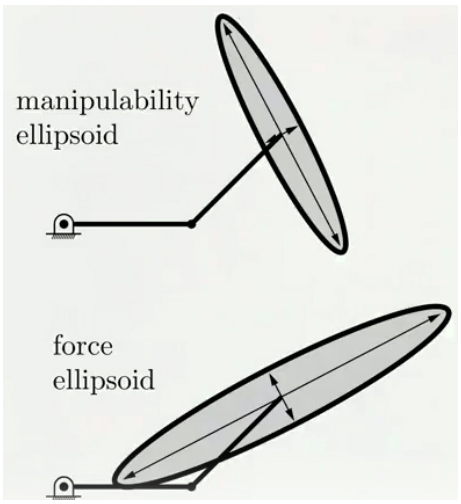

(a) Arbitrary force and manipulability ellipsoids for an RR robot arm

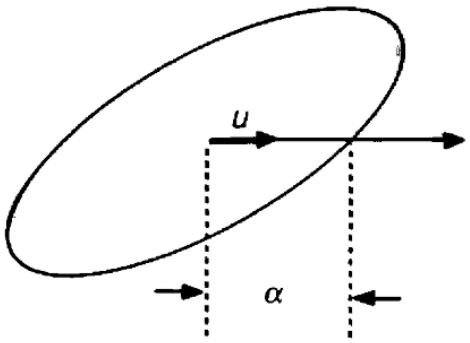

(b) Manipulability ellipsoid, task dependent directional vector ($\boldsymbol{u}$) and velocity transmission ratio (α)

Figure 2.1: Ellipsoids for manipulator performance evaluation

ative. The scope for manipulator performance indices can be split into intrinsic and extrinsic measures [3]. Intrinsic indices provide a measure of performance independent of the manipulators task or application - widely adopted metrics within this definiton include:

- Dexterity index [20]
- Condition number [21]
- Isotropy index [22]
- Manipulability index [23]

The latter, sometimes termed the Yoshikawa manipulability index (after its founder), is considered to have an advantage over some other measures due to being easily computable and expressed in terms of the robots joint angles. The index can be expressed as:

$$\mu(\theta) = \sqrt{det(\boldsymbol{J}\boldsymbol{J}^{\boldsymbol{T}})} \tag{2.1}$$

Where $\boldsymbol{J}$ is the Jacobian matrix for the manipulator, and $\boldsymbol{J}^{\boldsymbol{T}}$ its transpose. This μ value essentially describes the end-effectors proximity to a singularity, providing a scale for the isotropy of end-effector velocity given a set of joint parametres. A singularity is where the manipulator is entirely unable to carry out motion in the singular axis of the workspace coordinate system. A singularity will occur when the determinant of the manipulators Jacobian matrix is equal to zero. This can be visualized by considering the manipulability ellipsoid (Fig. 2.1a), whereby the volume of the ellipsoid is equal to the manipulability index and the shape of the ellipsoid

can be represented by the eigenvalues of the $\boldsymbol{JJ^T}$ matrix. There are also variants on Yoshikawa manipulability, such as relative and order-independent manipulability [22] which address some of the pecieved limitations of the manipulability measure such as the dimensional and frame dependency of the Jacobian matrix. The scalability of the manipulability measure can be addressed by normalizing the values (Fig. 2.2), where:

$$\mu_N(\theta) = \frac{\mu_i(\theta)}{max(\mu_1, \mu_2, \mu_3, ..., \mu_n)} \tag{2.2}$$

Analogous to manipulability is the force index which provideds a basis for analyzing

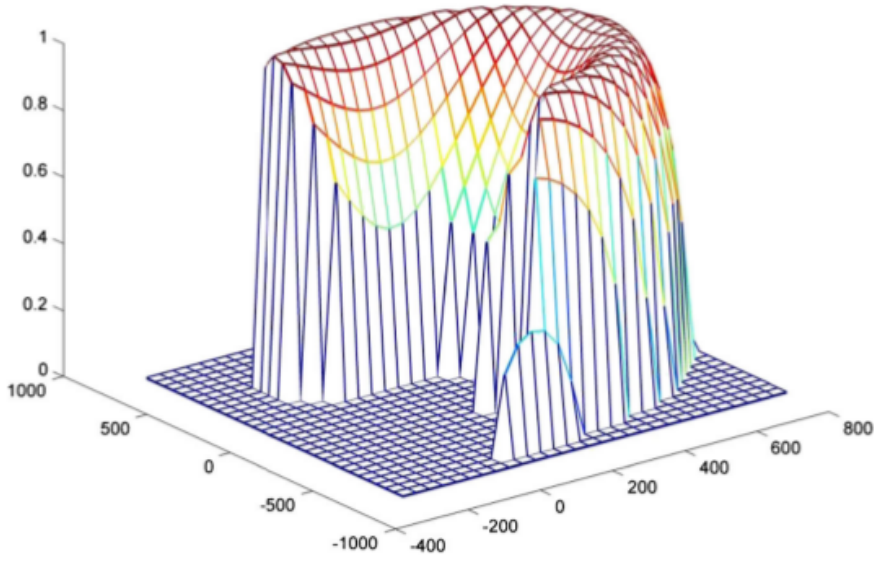

Figure 2.2: Distributed, normalized manipulability index for a SCARA manipulator [1], reproduced from Dr Tanio Tanev[2]

end-effector forces. The force transmission of an end-effector can be obtained by mapping the joint torques through the Jacobian transpose [24]:

$$\boldsymbol{\tau} = \boldsymbol{J^T f} \tag{2.3}$$

Thus, the force ellipsoid can be optained by considering the eigenvalues of the $\boldsymbol{(JJ^T)}^{-1}$ matrix; the inverse of the manipulability case. As shown in Fig. 2.1a, the force and manipulability ellipsoids are recipricol to each other. As a global measure, the GMI (global manipulability index) can be derived as the integral over the whole manipulator workspace:

$$GMI = \frac{A}{B}$$

Where A and B are equal to [1]:

$$A = \int_w (\mu)\, dW \quad and \quad B = \int_w dW$$

This provides a measure of consistent manipulability, where it would be favorable for a normalized manipulability GMI to stay above a given threshold for a given region. The intrinsic performance indices mentioned thus far are all common in that they are driven by the manipulator.

Extrinsic indices provide a measure of performance relative to the manipulators task or application. Chiu [25] recognized that manipulator tasks often require exerting a determined amount of force along a specified direction in space. A task-compatibility index was proposed, which accounts for the velocity and force transmission ratios (α and β) of a manipulator in the directional vector required by the task ($\boldsymbol{u}$), shown in Fig. 2.1b. The Chiu task-compatibility index can be expressed as:

$$c = \sum_{i=1}^{l} w_i \alpha_i^{\pm 2} + \sum_{j=l+1}^{m} w_j \beta_j^{\pm 2}$$

With α and β equal to:

$$\alpha = [\boldsymbol{u^T}(\boldsymbol{JJ^T})\boldsymbol{u}]^{-\frac{1}{2}}$$

$$\beta = [\boldsymbol{u^T}(\boldsymbol{JJ^T})^{\boldsymbol{-1}}\boldsymbol{u}]^{-\frac{1}{2}}$$

Where m describes the number of task coordinates with l force direction vectors and where w_i, w_j are weighting factors that indicate the magnitude and accuracy requirements.

The robot-task conformance index [3], is a dimensionless extrinsic measure which operates on the basis of four manipulability ellipsoids; the robot ellipsoid ξ_r, the task ellipsoid ξ_r and their affiliated $\xi_{\subseteq}$ $\xi_{\supseteq}$ ellipsoids which represent the largest contained and the smallest containing ellipsoid volumes respectively. This index builds on existing work for analysing ellipsoid intersection for the purpose of task-oriented manipulability measure [26]. Consider the volumes for these aforementioned conformance ellipsoids (Fig. 2.3), the robot-task conformance index is defined as a ratio of these volumes:

$$C_l = \frac{V_t}{V_{\supseteq}} = \frac{V_{\subseteq}}{V_r}$$

This index has the advantage of being independent of rotational and translation units and is well defined both within and outside the bounds of potential singularity. However, the measure is computationally intensive, thus Cloutier et. al defined a method for enhancing the index procedure by diagnolizing the task space. The index becomes the following:

$$C_{lt}^{(d)} = \sqrt{\prod_{j=1}^{m} \lambda_j}$$

A designer can use this index as an optimization criterion for an optimal interaction with the task-space.

The featured manipulator performance indices are applicable to a single, serial-chain robot and a single task space. A notable amount of research has been done on the optimization of manipulators working in parallel, sharing the same end-effector or tool point [27][28][24][29]. The performance indices in the parallel scenario, generally involve some derivation of the featured serial-chain indices. There are numerous other performance indices and tools for quantitvely evaluating robots, most of which are intrinsic, but those with largest traction have been mentioned. Generally speaking, the literature for intrinsic indices seems substantial in comparison to extrinic indices, this echos the design premise behind *most* robots; to efficiently multi-task. Some robotics researchers have even set to differentiate a 1DOF machine from a robot on the basis that it will be nonsuitable for performing multiple tasks [30].

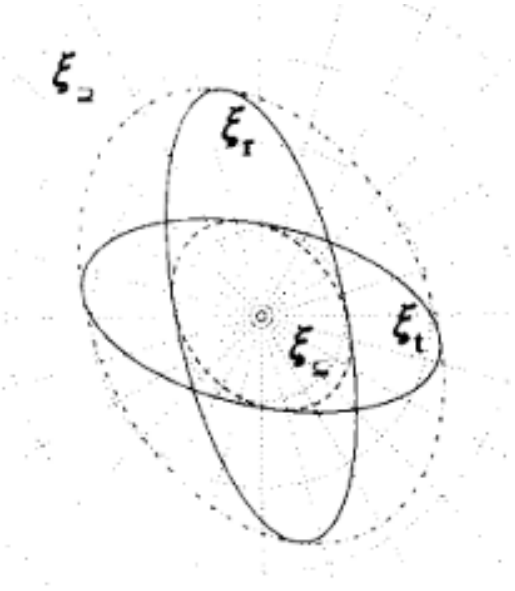

Figure 2.3: Superimposed robot-task conformance ellipsoids [3]

A relevant and simple result from this section is the manipulability of a Cartesian (X-Y-Z prismatic) axis robot. If we consider the task-space as a Cartesian coordinate system, then the forward kinematics of a Cartesian axis robot is simply the reflection of the joints. This means that the jacobian matrix for a Cartesian robot is simply equal to the identity matrix [31], and the eigenvalues for the $\boldsymbol{JJ^T}$ matrix are equal to one. Therefore, it can be concluded that a Cartesian manipulator is free of singularities within its workspace and will have a force and manipulability ellipsoid with all dimensions equal to one. Consequently, a real-world Cartesian axis robot with sufficient stiffness will have entirely isotropic force and velocity performance in a Cartesian task-space, whereas a rotational axis robot will not.

2.2 Harvesting robots

Many agricultural tasks such as harvesting, pollination, crop-maintenance etc. are typically repetitive and specific tasks. In order to be economically competitive with equivalent human labor, its is beneficial for an agricultural machine to complete tasks quickly, efficiently and reliably within environmentally challenging conditions. There are two main operational aproaches to the automated harvesting of produce; the first is to operate blind, the second is to operate selectively. Blind operation means that produce will be harvested via some method that does not rely on sensory input regarding specific fruit locations. An example of a harvesting machine that operates 'blindly' is an orange harvester [32], which shakes the citrus tree to detatch fruit from the stem. Blind, mechanical harvesting machines tend to be effective at quickly detaching fruit but often promote fruit damage - thus they are not suitable for many fruit types. Selective operation means that produce will be localized by some sensory input, and then harvested individually. Selective harvesting machines are generally classed as harvesting robots as they require a multi-disciplinary and dexterous approach for harvesting damage sensitive produce. A harvesting robot will typically consist of three main elements [33]:

1. A recognition system which identifies and locates produce
2. A picking system consisting of manipulator and detachment end-effector
3. Some movable platform which allows mobility through a growing system

A comprehensive review on 50 robotic harvesting systems found that the average harvesting robot would locate 85% of produce, detach 75%, harvest 66% and damage 5% [34]. Another important metric is harvest cycle time - this is generally the time taken to locate, detatch and harvest. The harvest cycle time is often one of the critical factors that influence economic viability of a system. The average harvest cycle time for published harvesting robot systems in 2014 was 33 seconds. Much of the technical challenges involved with robotic harvesting are well known [35][36][34][37], and mostly arise from task complexity in a dynamic environment.

One approach to improving harvestability and cycle times is to use an optimal hardware configuration. Henten et al. [38] had developed a successful cucumber harvesting robot but it was acknowledged their original manipulator kinematic structure was far from ideal. In-line with prior manipulator optimization methods [39], they used path-length and a variant of Yoshikawa manipulability measure as optimization criterion for the harvesting of cucumbers. Seven different, three-link,

manipulator configurations were evaluated; all of which were intended to act on a vertical prismatic link. It was found that the PPRR configuration returned the most favourable results. One study proposed the design optimization and simulation of the kinematic structure of an eggplant picking robot [40]. Optimized design parametres were the lengths of two of the four links on a 4R robot; the design objective was to cover a pre-defined workspace with the most compact mechanical structure. Another study [41], covered several topics essential for the design of a modular pepper harvesting and precision spraying robot. Detail on the kinematic design for this system was shown [42] by analyzing various high DOF (degree of freedom) work-space combinations in relation to the task-space. Normalized manipulability measure (Section 2.1) was used as a method for evaluating the relative performance of the robot at different locations. Despite the contributions mentioned, the majority of robotic harvesting systems focus their research on indentification and manipulator control instead of optimal hardware configuration. A related approach to improving harvest robot performance is from the grower-systems perspective; whereby developing a structured, less variable orchard architecture will allow for increased kinematic and machine vision performance [43].

As of 2018, there are a number of published, robotic harvesting systems across different crop types such as cucumber [44], sweet pepper[45], radicchio[46], tomato[47], strawberry[48], apples[49] and many others. However, despite the extensive research and development conducted thus far in the field of harvesting robotics; manual labour is still the economically favourable method for harvesting damage-sensitive produce. For this to change, robot harvestability percentages will need to increase and both damage rates and harvest cycle times will need to decrease. Unlike controlled manufacturing environments, whose processes lend themselves to cell-based generic multi-tasking robots, competent harvesting robots require a complex, task-specific approach to system development [50].

2.2.1 Multiple robot systems

Comparitive to many hands making light work of a human task; many robots provide a productivity advantage over a single robot. A loose definition for a robot is a mechatronic system with a manipulator and an end-effector. Going forward, and by that definition, this report will assume that a robot physically comprised of other robots is a multiple robot system. A multiple robot system can be differentiated from a group of robots whereby the former is a centralized system which introduces kinematic constraint between robots. Conversely, a group of robots may only be

constrained by their environment, structure and/or process.

With respect to harvesting robots, multiple robot systems provide an advantage over single robot systems by reducing the harvesting cycle time. Harvest cycle time can be reduced by a potential factor of N, where N is equal to the number of robots within the multiple robot system performing a harvesting task. However, this would assume parity of work distribution between the robots meaning 100% cooperative efficiency. In reality, equal work distribution between robots can be challenging to achieve, especially if there is a kinematic constraint such as all N robots mounted on a mobile platform. Thus, it becomes important to differentiate between single robot systems and multiple robot systems as the latter entails an additional set of challenges, to name a few:

- Task allocation and cooperative workspace management [51]
- Kinematics and localization for multiple workspaces
- Collision prevention

Multiple robot harvesting systems have been proposed for several years as a means to replace human labour. An economic analysis of robotic citrus fruit harvesting in Florida (1987), found that a multiple arm harvester capable of 85% harvesting efficiency and an average harvest cycle time of three seconds would be 50% more expensive than equivalent manual labour [52]. It was concluded that research and development was needed to improve harvesting efficiency, harvest cycle time and harvester cost; ironically these are still development challenges 30 years later. Following on from this (1993), an orange harvesting system was developed which used two, independent, electrically driven, telescopic robots - both mounted on a tracked platform vehicle [53]. Both robots used cameras within the end-effectors as opposed to mounted statically on the platform. 86% of oranges were successfully located and the harvest cycle time was reported as approximately 7.5 seconds for each arm. The orange harvesting sequence for the two robot arms was determined with a neural network based on the DTSP (double travelling salesman problem) where the shortest possible path between all oranges was obtained. It was concluded that the two most influencial variables affecting performance were lighting conditions and wind speed. It is not reported whether the two robot arms cooperated within a shared workspace or whether they operated simultaneously. Whilst the exact harvestability percentage was not given, the reported specifications achieved by this early 1990's system exceeds what was achieved, on average, as of 2014 [34]. With that being said, it is understandable that the literature on multiple robot harvesting systems is

still limited; generally speaking the challenges involved with single robot harvesting systems still remain very topical.

A more modern multiple robot harvesting system (Fig. 2.4) has been proposed for the harvesting of melons and for potential generic use. This system has evolved over time since its original conception over 20 years prior [54]. The system is essentially a rectangular frame that travels along a two-dimensional field at a constant velocity. Cartesian manipulators are mounted on the frame, each with a melon harvesting end-effector. The system is designed to operate dynamically, that is; the Cartesian robot-arms pick up melons whilst they are being towed along by a tractor. The Cartesian configuration of the manipulators allows for them to efficiently operate in the direction of tractor motion. This is due to the melon task-space geometry mapping particularly well in Cartesian space, matching the workspace geometry. However, because the harvesting is dynamic and the manipulators aligned in the axis of constant motion, the work distribution between robots does not constantly scale with number of harvesting arms [55]. Edan et al. do not present an explicit justification for adopting the Cartesian manipulator as opposed to a SCARA or other robot type. Interestingly, there has been an array of recent research associated with this system, some of which may be unique in the field of multiple robot harvesting systems. Most notably; harvest order planning for multiple robot arms [4], optimal motion planning for 2D crops [56] and performance analysis of multi-arm cartesian robot for fruit harvesting [57]. This research also has relevance to the field of kiwifruit harvesting as the crop types share a similar harvesting task-space geometry.

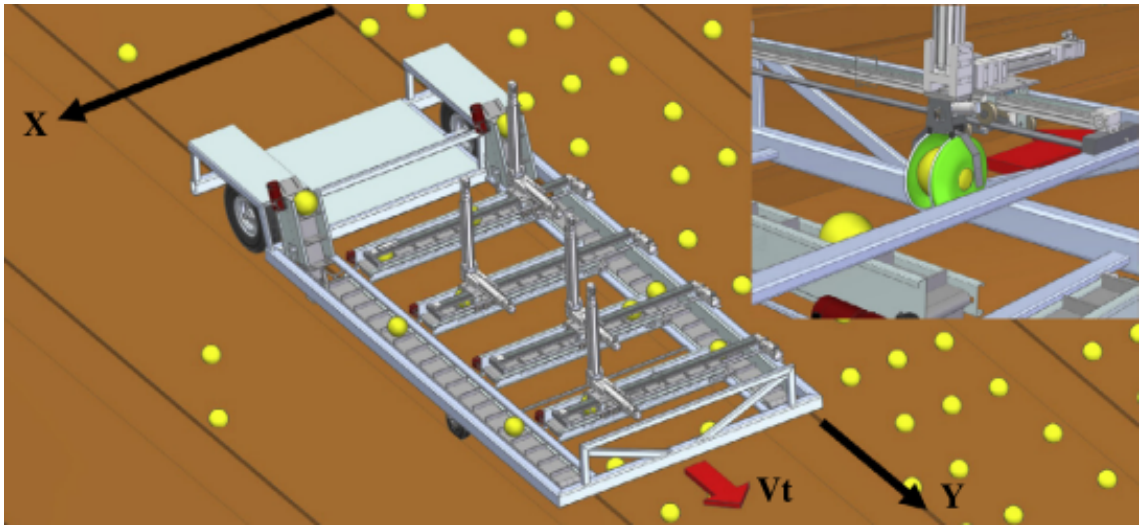

Figure 2.4: Cartesian axis multiple robot-arm system for the harvesting of melons [4]

A state-of-the-art multiple robot harvesting system has been developed by the company Agrobot [5] (Fig. 2.5). Published research on this system is not widely available, however, it appears to be one of the first of its kind - a multiple robot harvesting system which may soon be ready for commercial trial. Agrobot claim that the system is fully configurable for different strawberry row widths and consists of up to 24 robot arms. Another system which is advertised as being close to commercial trial is the Harvest Croo strawberry harvesting robot[58]. This robot appears to use 16 robot arms to pick strawberries in a similar fashion to the Agrobot. Claims from Harvest Croo are that the system will replace 30+ human pickers by harvesting 8 acres per day. Notably, both these systems adopt a similar Cartesian configuration for their regional manipulation structure, with some orientation method at the end-effector. The Harvest Croo robot uses a cartridge-style end-effector system which decreases the downtime involved with placing processing detached fruit.

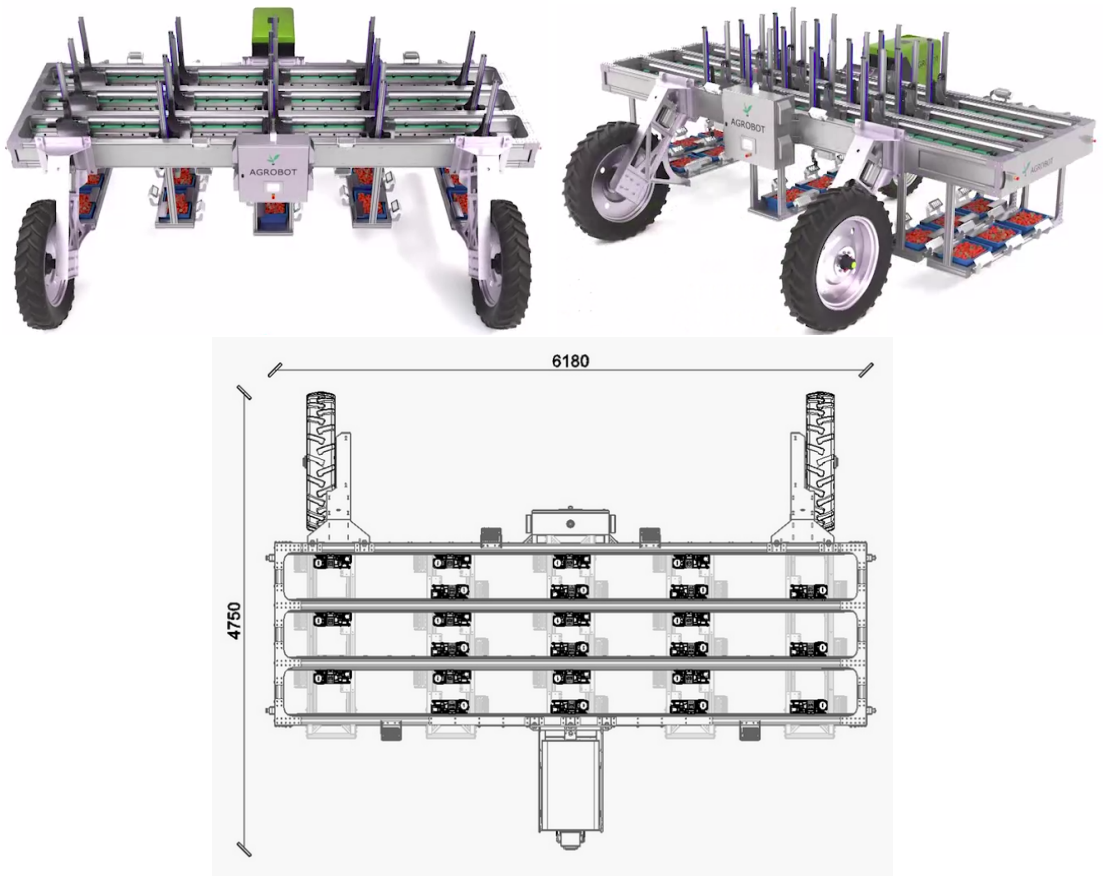

Figure 2.5: 2018 Agrobot E-series strawberry harvesting system [5]

2.2.2 Kiwifruit harvesting robots

There have been two significant kiwifruit harvesting robots, both of which were developed in New Zealand and act as pre-cursors to this research project [6][59]. Both systems were designed for autonomous use through pergola-style kiwifruit orchards. The task-space for kiwifruit harvesting is dictated by the pergola orchards and is best described as a 3D Cartesian system where X is the length of the orchard row, Y is the width of the orchard row and Z is the height variance of kiwifruit within the row.

Autonomous Kiwifruit Harvester (AKH)

Scarfe and his team from Massey University designed and built the AKH to address labor shortage in the kiwifruit industry. The AKH was a multiple robot system consisting of four articulated, planar RRR robot arms, each with a kiwifruit specific end-effector, mounted on an autonomous platform (Fig. 2.6). The project objective was to develop a commerically viable, autononomous kiwifruit harvester that would be capable of operating within variable and complex orchard environments. The four robotic harvesting arms on the AKH were specifically designed to mimic the harvesting action of a human. Localization and detection of fruit was done with stereopsis, image segementation and edge detection. The design brief for the system was to harvest four kiwifruit per second - considerably faster than harvest cycle times for other published harvesting robots at that time. The key results from the overall system as reported by Scarfe:

- 83.6% positive fruit identification
- 0.77 seconds per fruit per arm harvested in lab
- 1.43 seconds per fruit per arm harvested in orchard with asynchronous two-arm operation (0.72 seconds per fruit for the system)

The AKH was a significant achievement towards horticultural automation with an independant reviewer suggesting that the system was world-leading within its field. Scarfe claimed that the system configuration that he presented would resolve the slow harvest rates experienced by other systems. From a hardware perspective, the four robot arms were unable to syncronously operate in the orchard because of issues with cooperation. Cooperative, asynchronous results were described with two-arms - this suggests that the operating arms were those on the outsides of the machine

whose workspaces were no subset of each other. However, a method for solving collision was described by defining 'keep out' geometry in the X-Y plane. Also, the robot-arms would lose their location in space due to an increased force requirement of the picking end-effector. The resulting torques on the motor produced step-loss on the stepper motors. Scarfe suggested key improvements such as the additon of high intensity lighting, revised bin filling and closed-loop manipulator feedback would further enhance the AKH performance. The AKH served as an important development platform for robotic automation in the kiwifruit industry.

Multipurpose Orchard Robotics - Kiwifruit Harvesting Module (KHM)

The Multipurpose Orchard Robotics project is a four-year collaborative effort to extend upon Scarfes earlier work. An autonomous multi-purpose mobile platform (AMMP) was developed with the intention of harbouring different robotic modules dependent on seasonal requirements. Whilst most elements to this system such as machine vision, end-effector, manipulator etc. were iterative improvements over the original AKH, the design principles and layout remained similar with four RRR robot arms (Fig.1.2, 2.7). The 2017 MOR kiwifruit harvesting module achieved the following after a comprehensive test across three orchards:

- The system could harvest 51% of all kiwifruit
- 76.1% of fruit were localized by the machine vision system (89.6% of all reachable fruit)
- 24.6% of fruit were either dropped or knocked off by the end-effector
- Total average harvesting rate of 5.5 seconds per fruit (22 seconds per fruit per arm)

The 2018 version of the system included improvements to end-effector gripping hand and machine vision which resulted in 55.8% harvested fruit with only 8.7% knocked or dropped across two orchards and 12000 fruit. From an operational standpoint, the KHM harvesting process can be split into phases and sub-phases (the term 'cycle' was used in the paper but this has been modified to 'phase' to prevent ambiguity at a later stage in this report). A harvesting phase is the process whereby the AMMP stops, kiwifruit are detected and localized, the robot-arms attempt to harvest all reachable fruit, then the AMMP advances to a fresh, unharvested region of taskspace. The taskspace (orchard canopy) must remain static relative to the

workspace during harvesting to ensure there is no deviation in coordinate systems. It is important to define the phase-specific workspace of the KHM as the combined workspace of all four robot-arms when the AMMP is static. A sub-phase is the process where a robot-arm will move to a new fruit location and detatch the fruit from the canopy. Thus, a phase will be comprised of N sub-phases where N is the number of attempts at fruit detachment. N is not always equal to the reachable fruit within the static workspace because some fruit will require second attempts at harvesting, other times canopy occlusion will mean that some fruit reachable within a workspace cannot be detected and therefore are not harvestable. Harvesting the reachable fruit within an entire orchard would require approximately k phases where k is the number of times the entire taskspace volume is divisible by the KHM cycle-specific workspace when travelling in the direction of AMMP motion. However, Fig. 2.8 shows the plan view and cross-sectional side view of one KHM robot-arm workspace relative to the taskspace. Despite the relatively large volume and 650 mm dimension in the phase-advance direction, the irregular toroidal workspace geometry means that the actual phase-advance distance (or difference between static harvest regions) is only 300 mm due to the likelihood of missing fruit at various heights. Consequently, the short phase-advance distance means that the AMMP has to move more often and the machine vision system must detect and localize fruit more often. The detection alone took three seconds per image for the 2017 KHM system which was reported as a relatively large portion of the cycle time. Thus, operational down-time will increase with an increased number of phases per region of fruit. A workspace with a constant dimension in the phase-advance direction would be advantageous for decreasing down-time.

One important metric was the work distribution between the robotic arms during harvesting. It was found, across 3 orchards and 39 trial zones, that the average maximum discrepency in work distribution between the most active and least active robot-arm was 52.3%. In one of the trial orchards, the average minimum work of the least busiest robot-arm was 0%, whis suggests the robot-arms were cooperatively inefficient at harvesting the reachable fruit. This can be explained by the individual robot-arms on the KHM having a fixed, non-cooperative workspace of approx $\frac{1}{4}$ the volume of the phase-specific workspace (Fig. 2.7c). Most pergola kiwifruit orchards display a heterogenous distribution of fruit across the canopy. Therefore, without cooperative workspace between robot-arms, the distribution of work between them will scale inversely with heterogeneity of fruit distribution. Scarfe has previously proposed methods of operating the robot-arms in shared portions of their workspaces by utlizing collision prevention and cooperative scheduling. The com-

plexity involved with implementing these methods may not outweigh the potentially minimal returns which are inherently governed by the robot configuration.

A noteworthy statistic is the harvest cycle time of the KHM being 15 times slower than the cycle time of its previous iteration, the AKH, from nearly a decade prior. It is likely that the reported harvest cycle times of the AKH were intermittent, whereas the reported harvest cycle time of the KHM was indicative of full operation.

2.3 Summary

Firstly, it was found that a wide range of intrinsic and extrinsic performance indices exist for the qualitative performance measure of a robotic manipulator. These indices can be used in the development phase of a robot such that a near-optimal manipulator configuration can be achieved. A frequent indice component was the manipulator's representative jacobian matrix and the manipulabiltiy ellipsoid which reflects the relative motion and force capacity of a robot within its workspace. A basic and consequential conclusion was that a Cartesian (X-Y-Z prismatic axis) robot will have entirely isotropic force and velocity performance in a Cartesian task-space, whereas a rotational axis robot will not.

Secondly, after reviewing the current state of harvesting robotics, it was found that there are many systems in development across a wide range of crops with well known technical challenges. Key measures of efficacy were harvestability, fruit damage and harvest cycle time. Some research has been done on the kinematic optimization of harvesting robot manipulators in order to achieve better results. However, the majority focus remains on identification and control. A comprehensive review in 2014 found the average, published harvesting robot was capable of harvesting 66% of produce with 5% fruit damage and a 33 second harvest cycle time. One method of increasing this harvest cycle time is by employing multiple robot harvesting systems, which may reduce the harvest cycle time by N where N is equal to the number of robots within the system. There are few published multiple robot harvesting systems as the present challenges within single robot harvesting systems remain topical. One notable example of a multiple robot harvesting system was a melon harvester; this system employed a Cartesian axis configuration which allowed efficient spatial cooperation between manipulators in a Cartesian task-space. Associated research conducted with this system may prove relevant for the harvesting of kiwifruit due to the similar taskspace geometry. The Agrobot and Harvest Croo robots are likely the first harvesting robots to offer commercially viable specification.

Both systems adopt a Cartesian orientation structure.

Lastly, the combined AMMP mounted KHM is likely the world-leading kiwifruit harvesting robot in 2018. The development of this system, dating back to the original AKH, has focussed on key areas of kiwifruit harvesting such as fruit detachment, fruit identification and localization as well as the development of a robot-arm manipulator. A review of this system suggests that current hardware related limitations are; work distribution between robot-arms and phase-advance distance. Scaling to an integrated multiple robot system for commerical operation may benefit and/or require alteration of the kinematic structure to promote change in these areas.

2.3.1 Research Question

The objective behind this research project was to investigate whether there was a method of increasing the hardware performance of the KHM kiwifruit harvesting robot. An initial hypothesis was that transitioning to a prismatic axis system may increase hardware performance where the robot-arms would share a main axis for increased cooperation. After reviewing relevant topics it was found that Cartesian (X-Y-Z prismatic axis) systems have been previously adopted for the regional manipulation structure of successful multiple robot harvesting systems. However, methods for theoretical comparison or explicit justification for adopting a certain kinematic structure were found only on single robotic harvesting systems, not for multiple robot harvesting systems. This arrives at the following research question:

"Is a prismatic axis kinematic structure more effective than a rotational axis kinematic structure, for the multiple-robot harvesting of kiwifruit?"

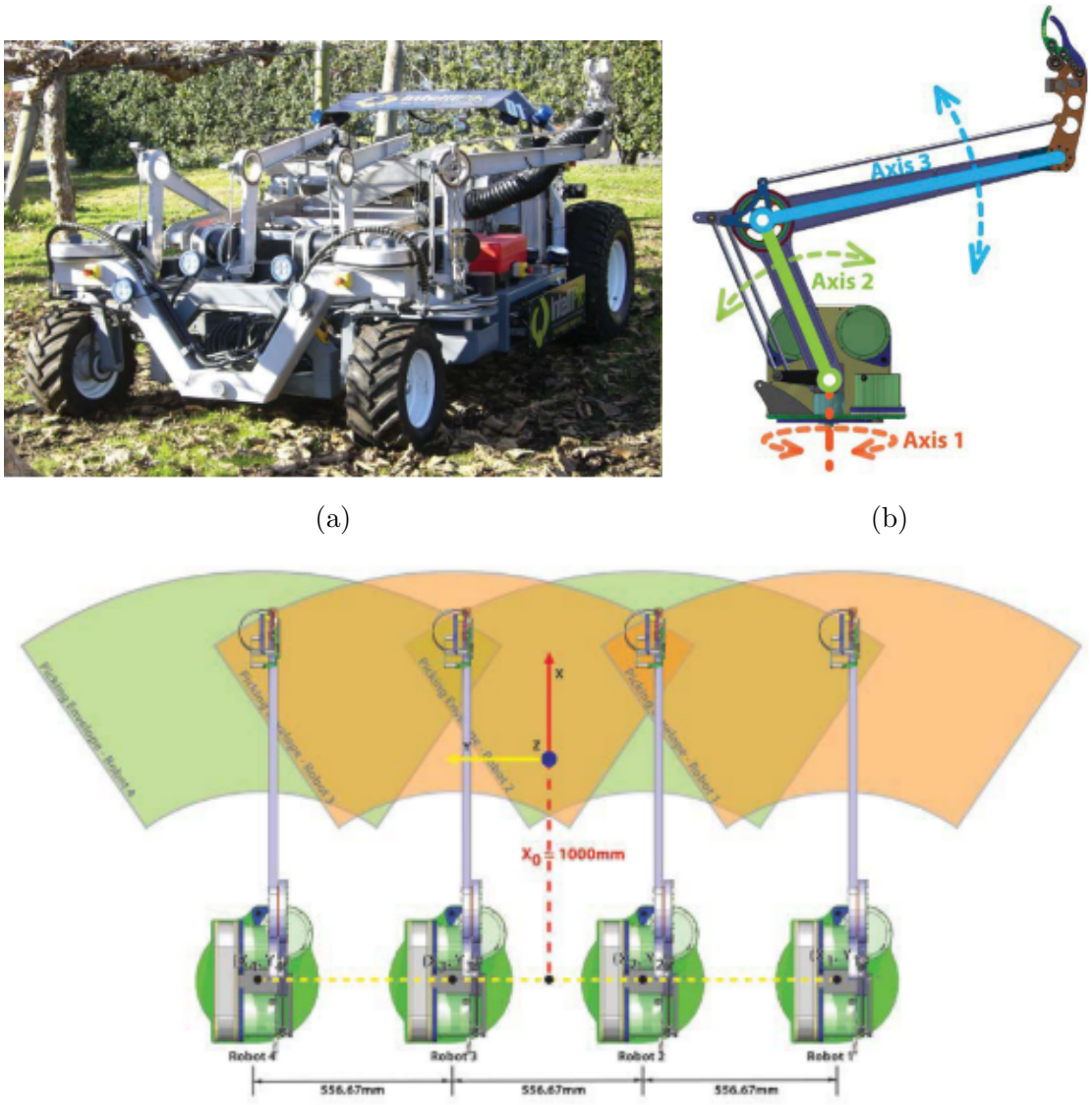

(a) (b)

(c)

Figure 2.6: (a) AKH system in orchard, (b) Robot arm configuration, (c) Workspace schematic of combined robot arms [6]

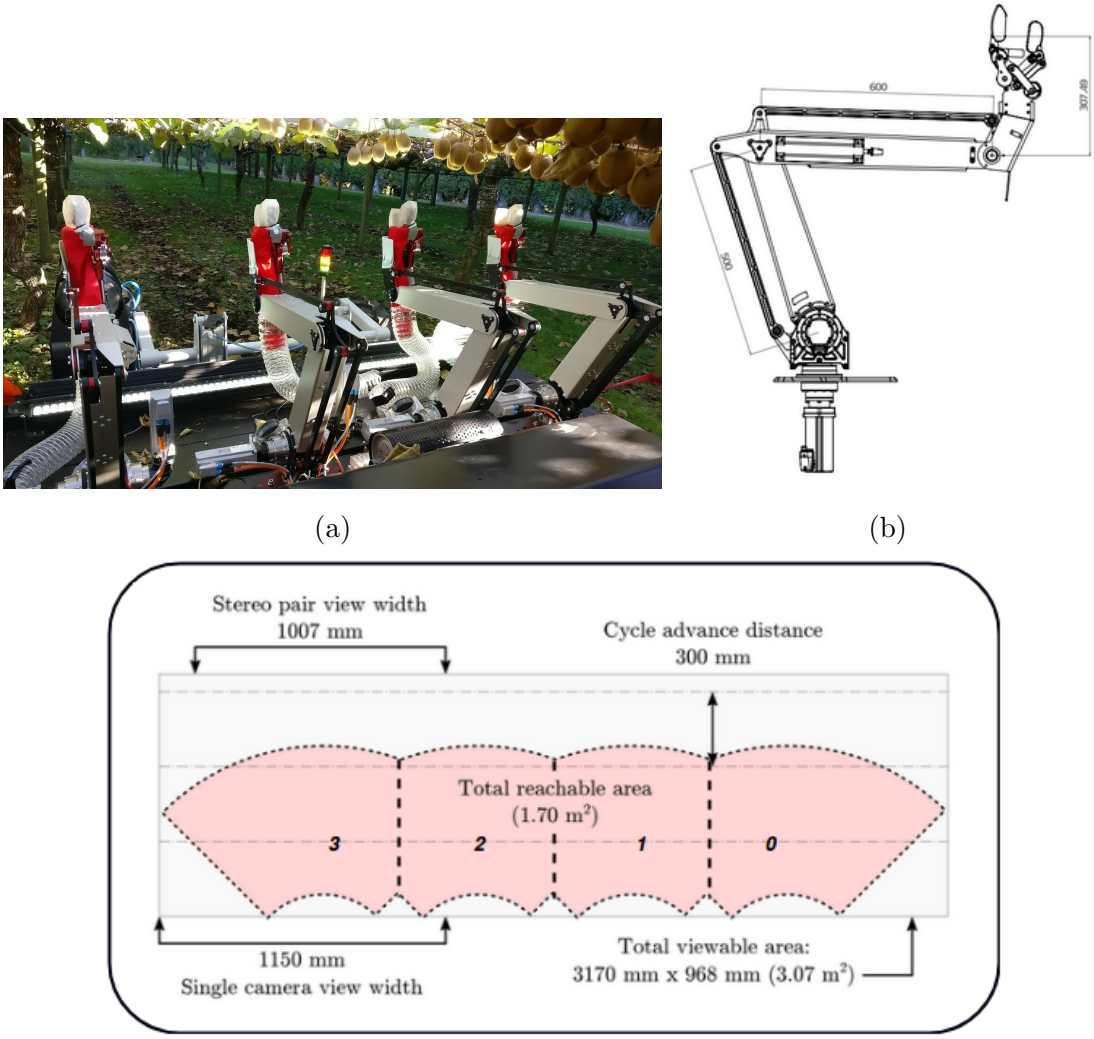

(a) (b)

(c)

Figure 2.7: (a) Harvest module in orchard, (b) Kiwifruit picking robot arm, (c) Cross-section of the KHM cycle-specific workspace at nominal fruit height

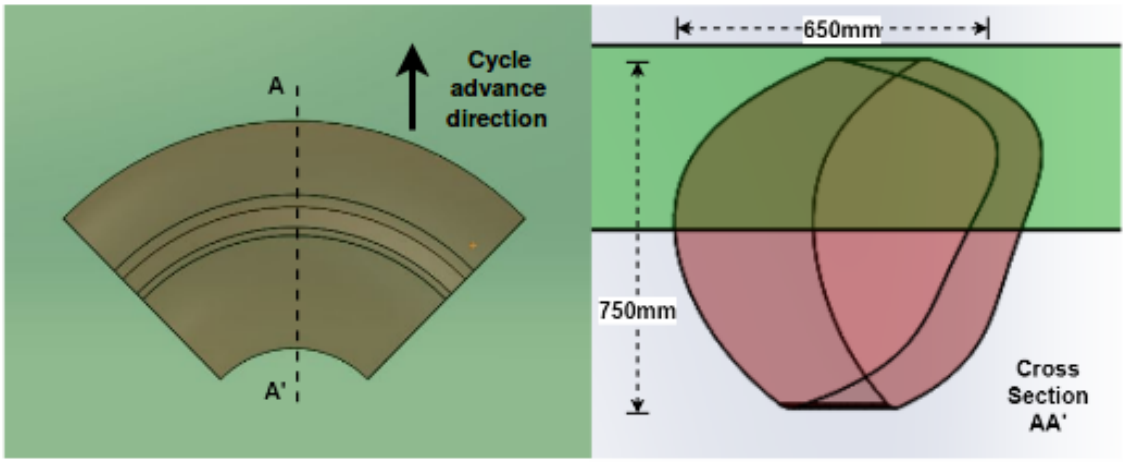

Figure 2.8: Centred cross-section of individual robot-arm workspace on the KHM

Chapter 3

Methodology

The prior chapter expanded on the research objective by reviewing relevant topics, a research question was proposed:

"Is a prismatic axis kinematic structure more effective than a rotational axis kinematic structure, for the multiple-robot harvesting of kiwifruit?"

The following chapter will aim to present a strategy and set measures for evaluating the research question.

3.1 Research strategy

A two robot-arm, prismatic axis kiwifruit harvesting robot will be designed, built, evaluated and compared to the original rotational axis system currently used on the KHM. Two robot-arms are an important consideration; in-line with the research question, it will become a multiple robot system whereby work distributions and other metrics specific to multiple robot systems can be evaluated. This prismatic axis (PPP) system will be Cartesian where each robot-arm has an X, Y and Z axis. The X axis on each robot will be common such that the robot-arms can move syncronously throughout a shared workspace. Each axis will be comprised of a linear rail system for motion constraint; the robot can be abbreviated LHR (linear-axis harvesting robot).

The preliminary stages of this process will be to create a design brief based on known limitations of the current system and of certain KPI's (key performance indicators) that have been used in other harvesting robotics evaluations and those relevant to kiwifruit harvesting. The development stage will include all mechanical, electrical and software design of the robot in approximately that order. When ready

for operation, the robot will be tested in the laboratory and in a kiwifruit orchard. Test measures will include quantitative and qualitative KPI's which will be defined in the following section.

Limitations of this method are that the evaluation relies on physical design which presents an array of variance and complexity. For example, will a disproportionate budget and component quality have influence on results? Are the design methods behind one system inferior to another, irrespective of the configuration that we want to test? In light of this, simulation could be a favorable method. Benefits of this method are that, if done properly, a tangible evaluation can be done on real-world systems with real world limitations such as manufacturing and physical component constraints. It is hoped that the prismatic axis kiwifruit harvesting robot developed as part of this research will allow for a non-bias evaluation but also act as an initial iteration for an alternative hardware approach.

The next section of this chapter will introduce evaluation and design measures based on harvesting robot KPI's. These measures will be topical throughout the development process. There will be a dedicated chapter for development and will include hardware design and control strategies (Chapter 4).

3.2 Evaluation and design measures

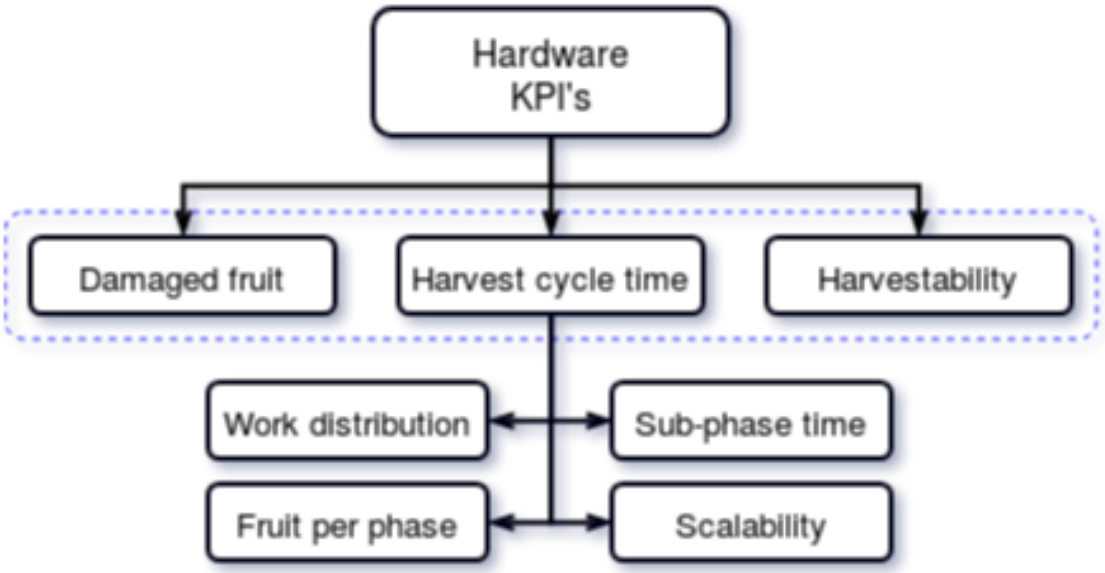

Figure 3.1: Hardware KPI map (key performance indicators) for a multiple robot kiwifruit harvesting system

Figure 3.1 shows a map of KPI's that will be used for evaluating and de-

signing the LHR. Only hardware measures have been condsidered as machine vision aspects exist outside the scope of this project. Those inside the blue bounding box are high-level KPI's and directly effect the economic viability and general performance of the harvesting robot. The lower level KPI's are constituents of the higher levels. The next sections will discuss why these high level KPI's are being used and how their constituents are relevant.

3.2.1 Harvest cycle time

Harvest cycle time was used as a measure of performance for all reviewed robotic harvesting systems. Harvest cycle time is important as it describes the rate at which the robot is able to work relative to manual labour. In the prior chapter, harvest cycle time was generally defined as the time taken to locate, detach and harvest a fruit. For the KHM, a phase was defined as the process where the AMMP moves to new region of task-space, the fruit are localized and the fruit are then harvested. A sub-phase is the act of the robot-arm selectively detaching and harvesting a fruit, then moving to the next fruit. By process analysis, the average harvest cycle time t_{HCT} of the KHM, with units of $\frac{sec's}{fruit}$, across a region of kiwifruit in an orchard can be expressed as:

$$t_{HCT} = \frac{t_{total}}{N_{fruit}} = \frac{N_{phases}}{N_{fruit}}(t_{move} + t_{locate} + t_{harvest}) \tag{3.1}$$

Where:

$$t_{harvest} = \frac{N_{fruit}}{N_{phases}} \frac{t_{sub-phase}}{N_{arms} W_D}$$

And where $t_{sub-phase}$ is the sub-phase time i.e. time between fruit. And W_D is a unitless work distribution constant. Thus Eq. 3.1 becomes the following:

$$t_{HCT} = \frac{N_{phases}}{N_{fruit}}(t_{move} + t_{locate}) + \frac{t_{sub-phase}}{N_{arms} W_D} \tag{3.2}$$

Equation 3.2 states that the harvest cycle time of the KHM across a region of kiwifruit is equal to the constant times involved with the harvesting phase throughout that fruit region, plus the sub-phase time when accounting for multiple arms. A further break down of this equation can be seen in Fig. 3.2.

In the review chapter, it was found that the KHM would benefit from hardware improvement in the following two areas: phase-advance distance and work distribution. Measures for both of these attributes can be found in the derived equation for KHM harvest cycle time; justifying that these are important elements for economic performance.

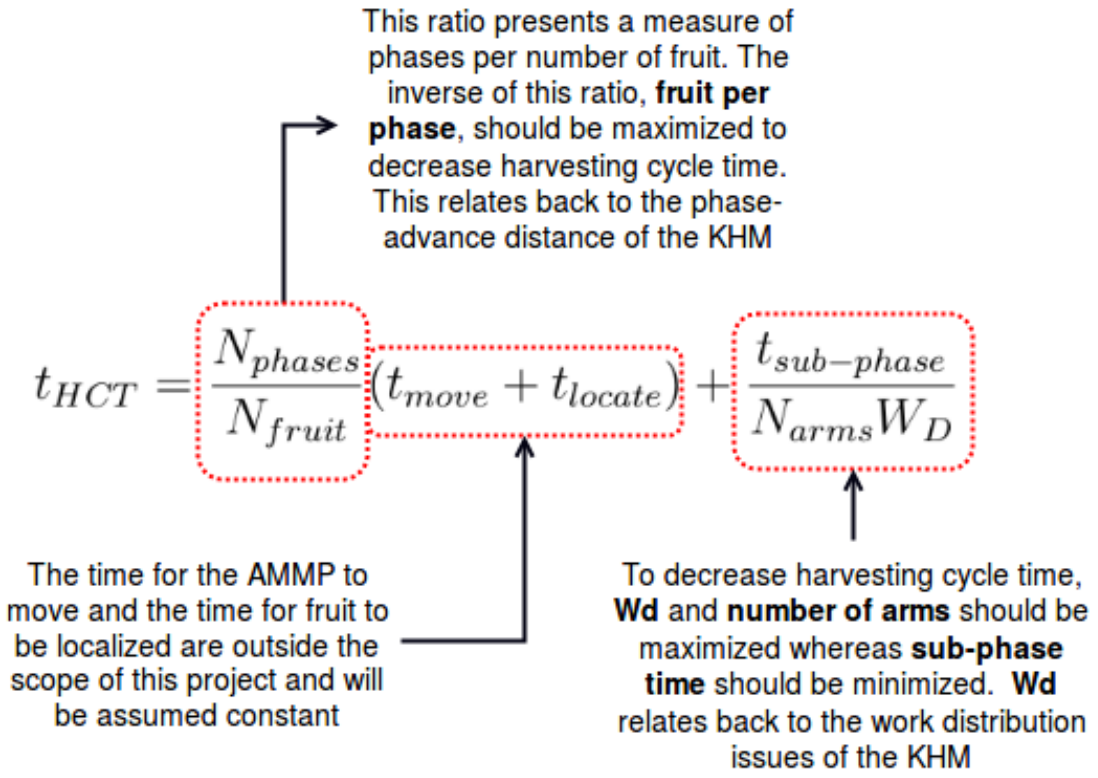

Figure 3.2: Break-down of harvest cycle time from Eq. 3.2

Work distribution

A constant W_D was proposed as a method for accounting for, and evaluating a work distribution between robotic-arms. W_D is essentially introducing a component of operational down-time to the harvest cycle time equation. This unitless, normalized constant is equal to the average theoretical work distribution at parity over the average work done by the busiest robot arm:

$$W_D = \frac{W_{parity}}{W_{busiest}} \tag{3.3}$$

The constant is defined as such because the busiest robotic-arm is what delays the system from progressing to the next phase. Maximizing W_D towards the value of one will decrease the harvest cycle time. An example - there are four robot-arms and five kiwifruit to pick, if one robot-arm picks two fruit whereas the other three robot-arms pick one fruit:

$$W_D = \frac{1.25}{2} = 0.625$$

If there are eight fruit and all the robot-arms each pick two fruit:

$$W_D = \frac{2}{2} = 1$$

The former example also displays one of the limitations of using W_D to evaluate performance as some tasks will be indivisible into the number of robot-arms and could unfairly sway averages. However, with an average canopy density of 40 $\frac{fruit}{m^2}$ [60], the granularity of work should be consistent enough between the phase-specific workspaces of the KHM and LHR to formulate a dependable W_D average. Another approach could be to weight the average with number of fruit per phase; however, that approach will not be taken in this report. Another measure of work distribution is the work discrepancy between the busiest and least busiest robot-arms. This measure had been used to evaluate the 2017 KHM work distribution and will be continued for comparison in this report.

Fruit per phase

The phases per fruit ratio describes the amount of KHM harvesting phases required to harvest a region of N fruit and can be seen in Fig 3.2. Consider the average volumetric density of fruit within an orchard, then the inverse - fruit per phase ratio, can describe the harvestable volume per phase. Hence, this fruit per phase ratio simply becomes volume per phase and is in direct relation to the phase-advance distance issue of the KHM. Maximizing this measure will cause the harvest cycle time to decrease by reducing the relative frequency of AMMP movement and identification/localization. The exact measure can be defined as simply; the harvestable taskspace volume per phase and can be denoted V_h. Thus, Eq 3.2 can also be written as:

$$t_{HCT} = \frac{t_{move} + t_{locate}}{\rho_v V_h} + \frac{t_{sub-phase}}{N_{arms} W_D} \tag{3.4}$$

Sub-phase time

The sub-phase time is the time taken for the robot-arm to selectively detach and harvest a fruit, then move to the next fruit. Minimizing the sub-phase time will decrease harvest cycle time (Fig. 3.2). There are several aspects that influence sub-phase time, some of these include:

- Motor/drive performance
- Path planning
- Distance between fruit (scheduling)
- Fruit damage and canopy disturbance

- End-effector fruit detachment
- The jacobian matrix of the manipulator
- Stiffness of the manipulator

In terms of making a comparison between systems, it in impractical to compare motor/drive performance as that is irrelevant to this research. Other elements on the list will all be qualitatively discussed during this report and quantitatively measured where possible. An initial hypothesis is that the sub-phase time of any kinematic structure will ultimately be limited by fruit detachment and the risk of causing fruit damage. Nevertheless, efforts will be taken throughout the development process to reduce sub-phase time.

Scalability

All other variables remaining constant, increasing the number of robot-arms on the KHM will decrease the harvesting cycle time. However, increasing the number of arms is not a fair measure by itself. Of interest is how the system will scale when increasing the number of robot-arms. For example, is the work distribution a function of the number of robot-arms? How many robot-arms can used within a fixed workspace? These are questions that will be qualitatively discussed, mathematical detail into these areas exists outside the scope of this report.

3.2.2 Harvestability and Damaged fruit

Harvestability is the measure of how many fruit can be harvested out of all available fruit, and is typically represented by a percentage. A large component of harvestability is software based, such as the ability to identify and localize the fruit. An equally important aspect is the hardware component which dictates how many of the fruit can be physically reached and successfully harvested by the end-effector with the required dexterity. There are several aspects that influence the hardware harvestability of kiwifruit, some of these include:

- Workspace and taskspace intersection
- Obstructed fruit (orchard cane, wiring)
- End-effector fruit detachment (especially amongst clustered fruit)

- Fruit orientation and manipulator dexterity
- Hardware tolerance i.e. the accuracy in which the end-effector can be placed in space

Harvestability on the LHR will be evaluated without the influence of machine vision and from a qualitative perspective. The hardware tolerance will be measured as part of a justification of the robot-arm kinematics.

The damaging of fruit directly affects the orchard owners profit margin from lost revenue, thus a measure of damaged fruit is another essential metric which will be considered on the LHR. In an attempt to minimize fruit damage, a novel end-effector will be developed on the premise of minimal interaction with fruit. No explicit trials will be done measuring fruit damage of harvested fruit (this exists outside the scope of this report); it will be assumed that all harvested fruit are non-damaged as a best case scenario and instead focus will be made toward the knocking or dropping of fruit as part of the end-effector detachment process. All kiwifruit that are knocked out of the canopy or dropped as part of end-effector detachment are considered rejects in industry, thus they are considered damaged fruit as part of this evaluation. The damaged fruit measures from the the LHR end-effector will be compared to the end-effectors trialled on the KHM.

3.3 Summary

To evaluate the research question, a two robot-arm, prismatic axis kiwifruit harvesting robot will be designed, built, evaluated and compared to the original rotational axis system currently used on the KHM. Each X, Y, Z axis on the proposed harvesting robot will be comprised of linear rails for motion constraint; thus the robot will be abbreviated LHR (linear-axis harvesting robot).

KPI's (key performance indicators) for the system were defined as harvestability, non-damaged fruit and harvest cycle time. The latter being further comprised by measures of work distribution, fruit per phase, sub-phase time and scalability. These KPI's will drive the design behind the LHR and also be used as qualitative and quantitative measures of evaluation.

Chapter 4

Development

This chapter will outline significant findings and processes arising from the development of a linear-axis kiwifruit harvesting robot (LHR).

4.1 Hardware design

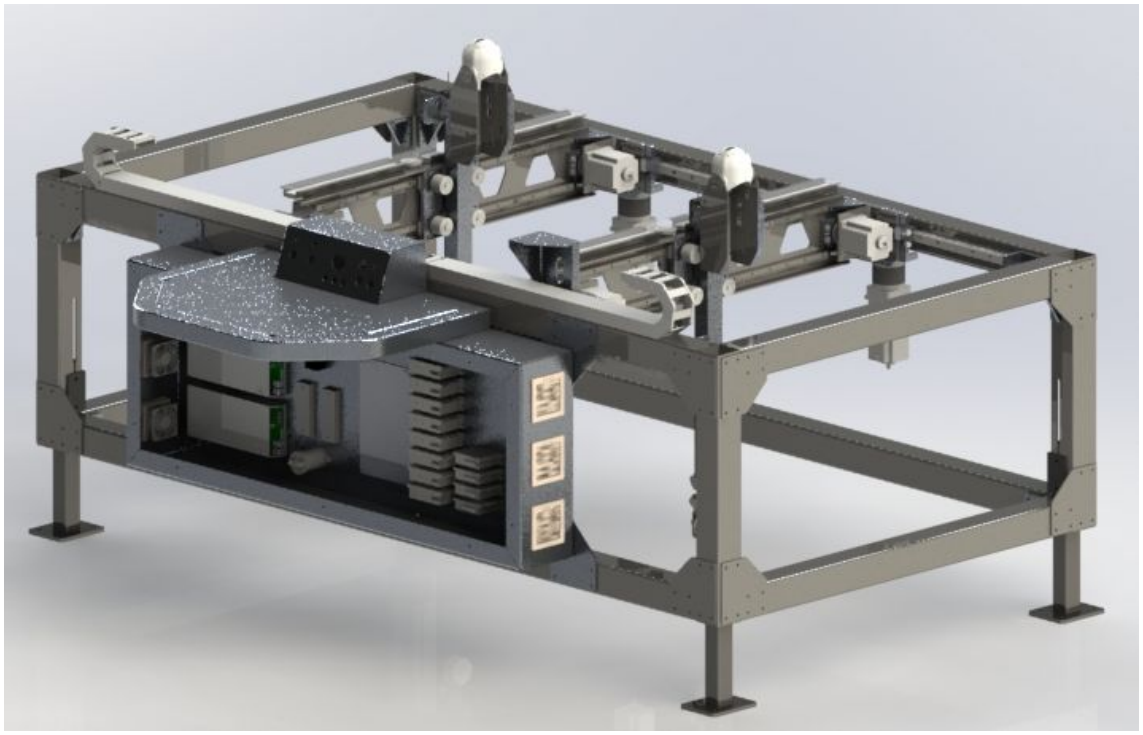

Figure 4.1: 3D CAD model of the LHR assembly

Inline with the evaluation and design measures from the prior chapter, the design brief for the LHR was to reduce harvest cycle time and fruit damage whilst increasing harvestablility. All mechanical design and modelling was done in the Solidworks 3D CAD program.

4.1.1 Manipulator

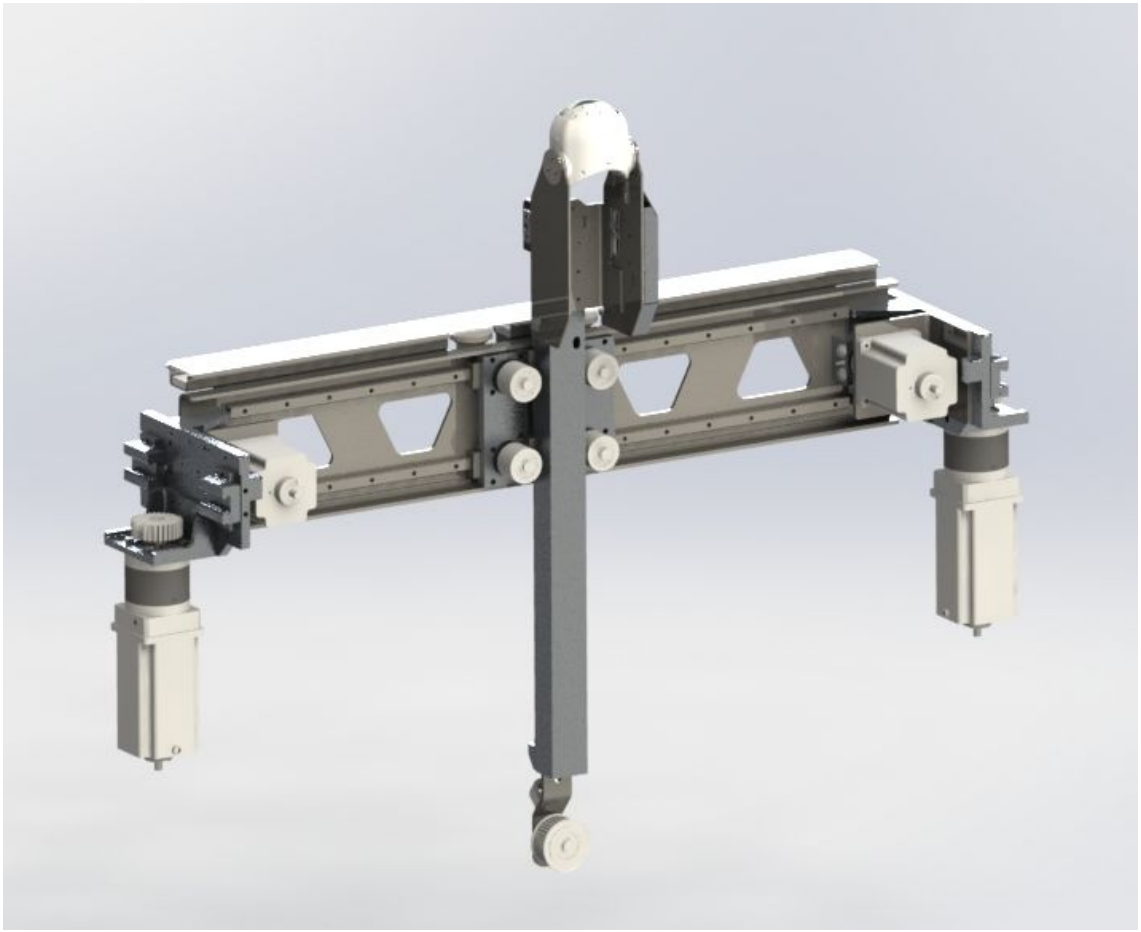

Figure 4.2: 3D CAD model of a differential drive LHR robot-arm, without timing belt

There were many details involved with manipulator design and not all of them will be covered here. However, two critical design considerations were found that factor into the wider efficacy of the system - those considerations will be covered in this section along with the proposed design solution and some of its features.

Carriage length

The two robot-arms on the LHR share the same X axis which is constrained by a linear rail on both sides of the machine. The X axis drive on each robot-arm is provided by a rack and pinion also on both sides of the machine. The shared X axis means that a large portion of the workspace for each robot-arm is shared. The degree to which the workspaces are shared depends on the robot-arm width in the X direction. As an example: for a shared rail length A, if the robot-arm width $x = \frac{A}{4}$ then the workspace for each robot-arm is $A - 2x = \frac{A}{2}$ and the maximum

cooperative workspace is $A - 3x = \frac{A}{4}$. For maximum workspace and prospective cooperation, the robot-arm width should be as small as possible. One of the limits to

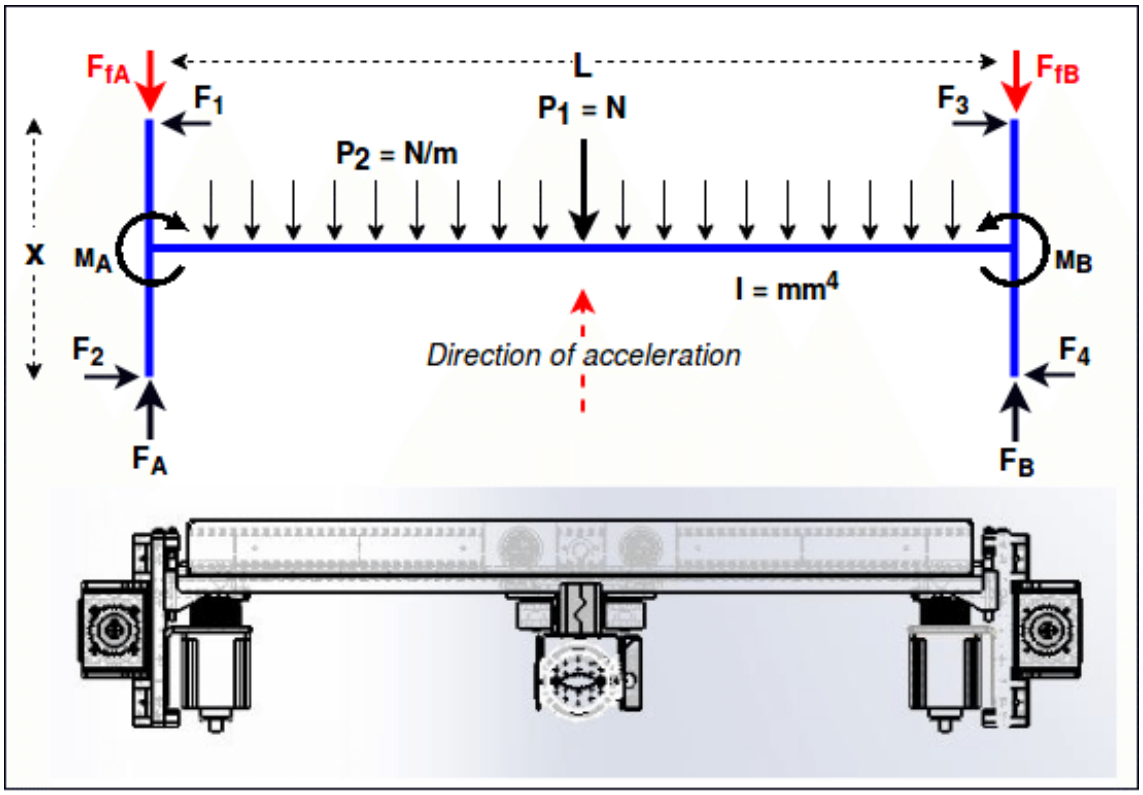

Figure 4.3: Plan-view loading on LHR robot-arm carriages

the robot-arm width is the space needed for components i.e. end-effector, cameras, motors etc. Another limit is the carriage length. Each side of the robot-arm has a carriage which consists of two linear bearings that provide motion constraint along the linear rails. Going forward, this report will assume the carriage length is the distance between the linear bearing centers on the carriage. Figure 4.3 shows the plan-view loading of an LHR robot-arm with the carriage length denoted x. When accelerating along the X axis, moments are induced at each carriage. The sum of moments around carriages A and B must equal zero $\sum M_A = \sum M_B = 0$, thus reaction forces are present F_{1-4} between the carriage's linear bearings and the linear rail. However, these reaction forces produce a frictional component which can be deterimental to the X axis motion. The total friction force on carriage A (F_{fA} in Fig. 4.3) includes the contribution from moment reaction forces $F_{fA_{reaction}}$ and also the contribution from gravity $F_{fA_{gravity}}$. The contribution from gravity is only a function of friction coefficient and mass, however the reaction contribution is also a function of acceleration and carriage length:

$$F_{fA} = F_{fA_{gravity}}(\mu_f, m) + F_{fA_{reaction}}(a, x, \mu_f, m)$$

Moments around A can be summed as follows when considering the worst case for F_1 and F_2 is when the YZ carriage (point load P_1) is positioned at $\frac{L}{2}$:

$$\sum M_A = 0 = (F_1\frac{x}{2} + F_2\frac{x}{2}) - (\frac{P_1 L}{8} + \frac{P_2 L^2}{12}) \tag{4.1}$$

Then the definition for the moment reaction friction force:

$$F_{fA_{reaction}} = \mu_f(F_1 + F_2) = \frac{2\mu_f}{x}(\frac{P_1 L}{8} + \frac{P_2 L^2}{12}) \tag{4.2}$$

When considering that the loads P_1, P_2 are masses (m_1, m_2) subject to an acceleration a, Eq. 4.2 can be written:

$$F_{fA_{reaction}} = a\gamma \tag{4.3}$$

Where:

$$\gamma = \frac{2\mu_f}{x}(\frac{m_1 L}{8} + \frac{m_2 L^2}{12}) \tag{4.4}$$

Thus, the total friction force on carriage A can be expressed as:

$$F_{fA} = \frac{\mu_f mg}{2} + a\gamma \tag{4.5}$$

The drive force on carriage A, provided by the rack and pinion, is denoted F_A in Fig. 4.3. To accelerate the robot at a:

$$F_A = \frac{ma}{2} + F_{fA} = \frac{\mu_f mg}{2} + a(\frac{m}{2} + \gamma)$$

And for the total drive force on the robot F_{drive}, where $F_{drive} = F_A + F_B$:

$$F_{drive} = \mu_f mg + a(m + 2\gamma) \tag{4.6}$$

The gravity friction component $\mu_f mg$ will generally remain constant (although μ_f *can* vary slightly with velocity) and can be offset by a constant force, independent of acceleration. However, moment reaction friction force must be offset by a drive component which increases linearly with acceleration. This model is based upon an ideal rigid body, in reality there can be internal stresses, misalignments and robot-arm deflections which can increase the γ factor. In the worst case, if the 2γ factor is not accounted for and exceeds the value of the robot-arm mass, the robots motion can bind; inhibiting X axis motion entirely. Furthermore, the components of F_{1-4} can exceed the Y axis loading capacity of the linear bearings if γ gets too large, independent of μ_f. This can cause wear and/or bearing failure.

In summary, the LHR robot-arm γ value can be deterimental to the drive performance by increasing friction. γ can be reduced by reducing masses m_1 m_2, robot-arm length L and friction coefficient μ_f. Reducing the carriage length can help to reduce the robot-arm width for increased workspace efficiency, but in doing so the γ value will increase.

Minimizing deflection

The end-effector is the most distal part of the LHR robot-arm, especially when the Z axis is extended. The stiffness of the robot-arm will dictate the degree to which the end-effector will deflect out of position during motion. This is not critical to end-effector performance as the end-effector will only actuate once the robot-arm is static, however, is it advantageous for the system to be non-compliant and under minimal stress during operation. Insufficient stiffness and component strength can also cause unwanted vibrations which can attribute toward cyclic loading and ultimately failure. Non-compliance under load can also decrease accuracy and introduce static settling times which slow the sub-phase time. To account for this during LHR development, an expression was derived for maxmium deflection through the end-effector load path during peak acceleration (dynamic response is outside the scope of this report). Figure 4.4 shows a free-body diagram of the side-view loading on the LHR robot-arm, with the end-effector location indicated by point E. Similar to

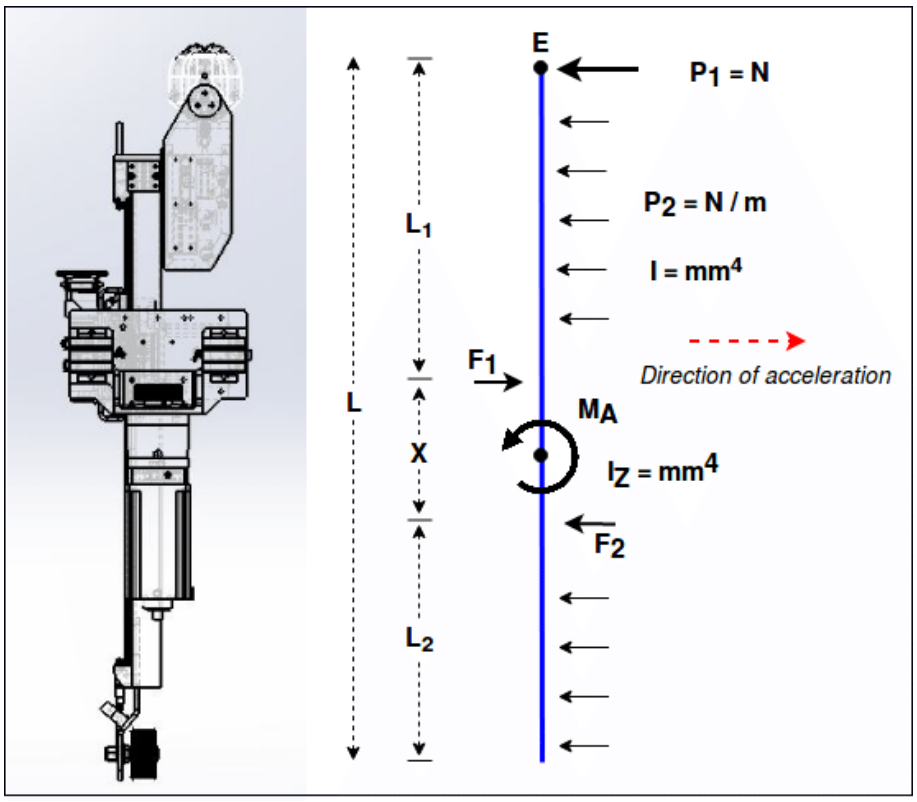

Figure 4.4: Side-view loading on vertical axis of LHR robot-arm

the X-axis motion constraint, motion in the Y axis is constrained by a pair of static linear rails with two pairs of linear bearings on a common, dynamic carriage. Motion in the Z axis is constrained by two static linear bearings and a dynamic linear rail. Acceleration of the robot-arm in the X axis induces a moment about the center of

constraint. Moments about this point must be equal to zero $\sum M_C = 0$, thus reaction forces are present F_{1-2} between the static linear bearings and the linear rail. By using the principle of superposition, the deflection at E for small deflections can be modelled as contributions from the UDL (uniformly distributed load) P_2, from the end-effector point load P_1 and from the torsional deflection about the center of constraint:

$$\delta_E = \delta_{E_{P1}} + \delta_{E_{P2}} + \delta_{E_{twist}} \tag{4.7}$$

In Fig 4.4 the worst case deflection scenario of E is when $L_2 = 0$ and $L_1 = L - x$, and when torsion acts on the centre of the Y axis $\frac{L_Y}{2}$. Thus max deflection $\delta_{E_{max}}$ can be expressed:

$$\delta_{E_{max}} = \frac{P_1 L_1^3}{3EI} + \frac{P_2 L_1^4}{8EI} + (L_1 + \frac{x}{2}) tan(\theta_{twist}) \tag{4.8}$$

Where:

$$\theta_{twist} = \frac{M_{12} L_Y}{2JG}$$

Equation 4.8 assumes a fixed support cantilever deflection over the span L_1 by P_1 and P_2, it also assumes a consistent torsional constant J about the length of the robot-arm L_Y. Equation 4.8 can be expanded when considering the definition of M_{12} as the moment supported by the force couple F_1 and F_2, and that the loads P_1, P_2 are masses (m_1, m_2) subject to an acceleration a:

$$\delta_{E_{max}} = a(\frac{m_1 L_1^3}{3EI} + \frac{m_2 L_1^4}{8EI}) + (L_1 + \frac{x}{2}) tan[(\frac{aL_Y}{2JG})(\frac{m_2}{2}(L_1 + \frac{x}{2})^2 - \frac{m_2}{2}(\frac{x}{2})^2 + m_1(L_1 + \frac{x}{2}))] \tag{4.9}$$

If variables such as L_1, L_Y are considered fixed as workspace requirements, and that m_1 is fixed as a required end-effector mass. Then $\delta_{E_{max}}$ depends on the mass-specific stiffness $\frac{EI}{m}$ of the Z axis element, and on the torsional rigidity JG of the Y axis element. Reducing the M_{12} reaction forces by reducing mass along the Z axis also means that lower capacity linear carriage/rails can be used - further decreasing mass. Optimizing for these properties will reduce the deflection of the robot-arm such that greater accelerations can be achieved for a given deflection specification. Greater permissible accelerations will decrease the sub-phase time on the LHR.

Differential drive solution

A differential drive (Fig. 4.5) was used as a method of increasing workspace efficiency by reducing robot-width and decreasing sub-phase time by minimizing deflection and inertia.

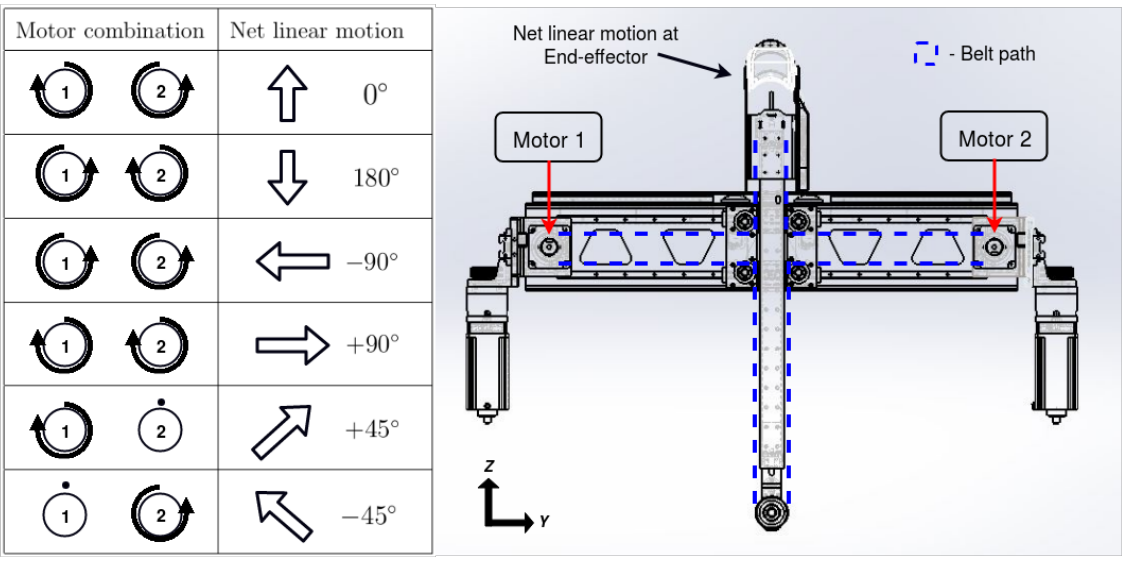

Figure 4.5: Schematic showing differential drive principle on LHR robot-arm

The differential belt drive configuration uses a single timing belt, driven by two motors located at opposite ends of the Y axis stroke, both of which contribute to YZ planar motion of the end-effector by changing belt proportions in each axis. Figure 4.5 shows the working principle of motion; the free ends of the belt are fixed on the upper Z axis element such that when a single motor rotates there is an even extension in both the Y and Z axis causing a 45° motion vector. These vectors can be represented by T_1 and T_2. When both motors rotate at the same speed the end-effector's net motion vector will be in the Y or Z axis depending on motor direction. More complex paths are achieveable when differing the velocity and acceleration components of each motor; hence differential drive.

The advantage of this system is that the YZ drive motors do not contribute to the Y or Z axis inertia and can be positioned on/close to the X axis carriages. When considering the mass of the YZ drive motors is equal to approximately 75% of the mass of the other Y and Z axis machine elements, acceleration in those axis' is improved by over 40% by having the motors estranged from motion. Furthermore, if the motors were part of the Y axis dynamic mass, they would introduce point loads which would increase momentary reaction around the X axis carriage - increasing the γ value. If also part of the Z axis dynamic mass, they would introduce point loads that would increase deflection; requiring greater stiffness and torsional rigidity which would likely require the addition of more mass. Therefore, it is exponentially beneficial to locate mass proximal to the X axis carriage centers.

The inverse kinematics behind the LHR robot-arm can be derived from two linear transform matrices. The first matrix in Eq. 4.10 shows the relationship

between the three linear output axis' of the LHR $X^{'}$, T_1, T_2 and the Cartesian taskspace axis' X, Y, Z.

$$\begin{bmatrix} X^{'} \\ T_1 \\ T_2 \end{bmatrix} = \begin{bmatrix} 1 & 0 & 0 \\ 0 & -1 & 1 \\ 0 & 1 & 1 \end{bmatrix} \begin{bmatrix} X \\ Y \\ Z \end{bmatrix} \tag{4.10}$$

Equation 4.11 shows the relationship between the LHR drive motor rotations $\theta_{X'}$,θ_{T_1},θ_{T_2} and the LHR linear output axis':

$$\begin{bmatrix} \theta_{X'} \\ \theta_{T_1} \\ \theta_{T_2} \end{bmatrix} = \begin{bmatrix} \alpha & 0 & 0 \\ 0 & \beta & 0 \\ 0 & 0 & \beta \end{bmatrix} \begin{bmatrix} X^{'} \\ T_1 \\ T_2 \end{bmatrix} \tag{4.11}$$

Where α and β are conversion constants dependent on pinion and pulley geometry respectively. The matrix in Eq. 4.12 shows the relationship between LHR drive motor rotations and Cartesian taskspace axis' as a product of the two prior transforms.

$$\begin{bmatrix} \theta_{X'} \\ \theta_{T_1} \\ \theta_{T_2} \end{bmatrix} = \begin{bmatrix} \alpha & 0 & 0 \\ 0 & -\beta & \beta \\ 0 & \beta & \beta \end{bmatrix} \begin{bmatrix} X \\ Y \\ Z \end{bmatrix} \tag{4.12}$$

This kinematic equation was verified by in-lab testing (Fig. 4.6). The constraint of linear motion was an important feature of the LHR. Linear bearings are generally available as plain bearings or as rolling-element bearings. Plain linear bearings, or linear bushings, rely on sliding contact between the bearing and the rail surfaces and are typically made from low friction polymers. Rolling-element linear bearings use recirculating, or non-recirculating balls or rollers between two bearing surfaces. Plain bearings are advantageous for a field-based harvesting robot because of their ability to withstand shock loads, vibrations and harsh environments. The main advantage is that plain linear bearings can operate without comprise if material/particulate enters between the bearing and the rail, a linear ball bearing can fail catastrophically in this scenario. However, plain polymer-based linear bearings have a typical friction coefficient of around $\mu_f = 0.2$, whereas the linear ball bearing value is approximately $\mu_f = 0.005$. Therefore, linear plain bearing adoption for the X axis carriages would increase the γ value (Eq. 4.4) and static friction values by

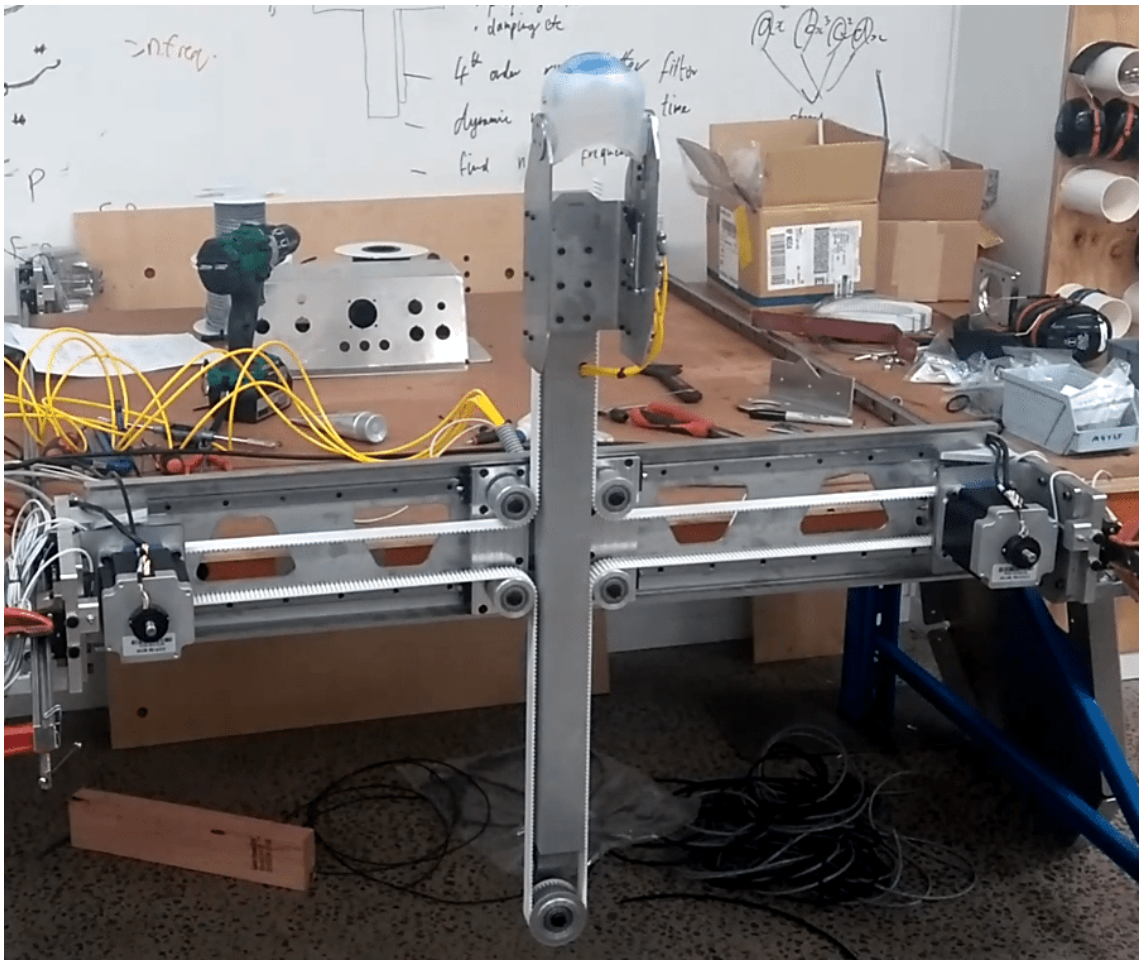

Figure 4.6: Initial assembly and kinematics testing of LHR differential drive with end-effector

a factor of 40 over a ball bearing; decreasing drive efficiency and limiting carriage length. The resultant design decision was to opt for linear ball bearings with large seals to help prevent debris ingress.

Recirculating linear ball bearings must retain tight tolerances with the ground rails in which they travel along, consequently they are very rigid and require accurate alignment - this was the main focus behind much of the design on the LHR. The X and YZ axis carriages (Fig. 4.7) were multi-part, jig-fit assemblies made from 6061-T6 Aluminium and machined to ISO 2768-1 tolerance [61] to ensure alignment. The sheet metal used for the Y axis body was laser-cut 304 Stainless Steel. Despite the increase in weight over Aluminium, the added strength and rigidity increases dimensional consistency. Despite the emphasis on mass reduction, it was deemed more important that the assembly was non-compliant; using ball bearings instead of plain contributed to this trade-off. To reduce weight, material was removed from regions of the Y axis body that were sufficiently distant from the fold lines to prevent

the relief of residual stress which could cause deflection. All connections throughout the LHR robot-arm load path were bolted, with planar adjustment at the ends of the Y axis body to account for any misalignment.

Drive on all axis of the LHR was provided by stepper motors. Stepper motors were chosen as they provide cost-effective accurate positioning. One of the downsides to using stepper motors is they can lose position during motion when subject to opposed torque. Stepper motors can also lose position through a mismatch of load and rotor inertia causing excessive resonance amplitudes [62]. This was of large concern on the X axis drives as there was an interia ratio of 50:1 and any imbalance between the opposite carriage drives could increase the likelihood of binding. To account for this, a 4:1 gearbox was used on the X axis drives which reduced the influence of load inertia by a factor of $4^2 = 16$. Acetal pinion gears were also used to introduce elasticity into the drive coupling; reducing resonance. Furthermore, each motor had positional feedback from an encoder so that if position loss became problematic the motion controller could account for the change.

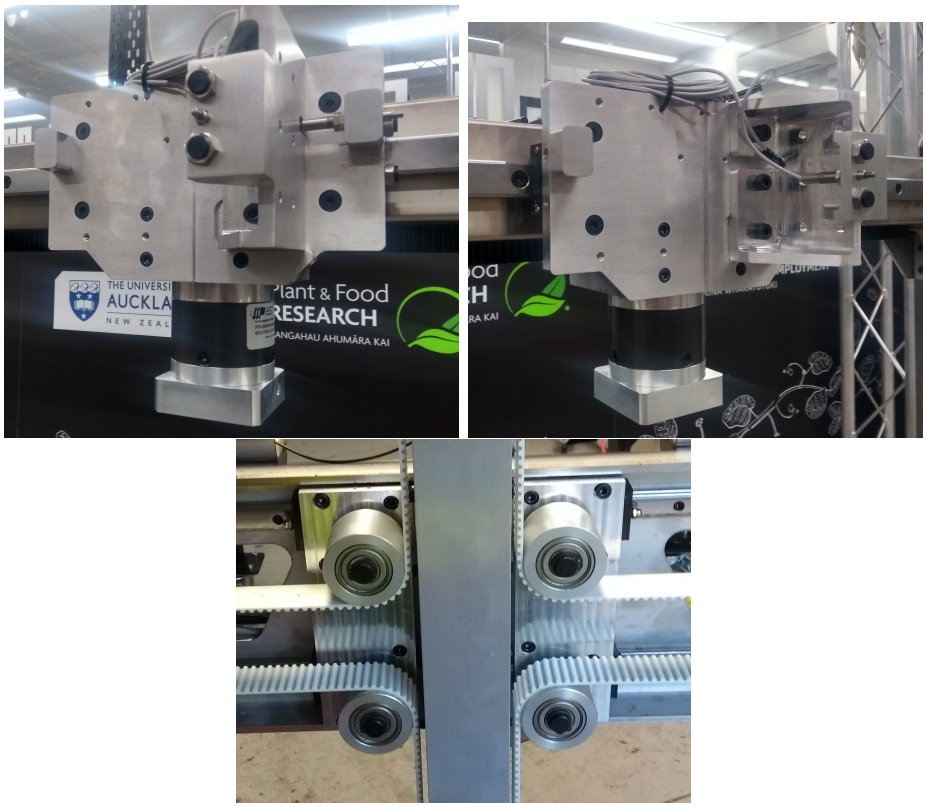

Figure 4.7: X and YZ axis jig-fit carriage assemblies on the LHR, designed with an emphasis on alignment

4.1.2 End-effector

The end-effector used by Williams et al. [59] grips and rotates the fruit in a similtaneous motion which is seen as an effective and time-efficient method of detachment. As the end-effector is unactuated and grip force relieved, the detached kiwifruit drops into a tube and onto a conveyor; this means that the robot-arm can continue to the next fruit without needing to place the fruit after detachment. It was found that the end-effector used by Williams et al. was partially responsible for the dropping of approximately 16% of fruit during the detachment process. The accuracy of the machine vision system also contributed to the amount of dropped fruit. In light of this, a novel end-effector concept was developed for the LHR in an effort to decrease fruit damage and increase fruit harvestability. This section will briefly cover the end-effector development process.

Trained, human kiwifruit pickers detach the fruit from the canopy by rotating it about the axis perpendicular to the stem, this creates a shear force at the fruit-stem connection; detaching the fruit. The fruit-stem connection is much better at withstanding axial load than shear loading, hence if the kiwifruit are pulled straight down along the stem-axis, the weakest point along the load path is often the stem-branch connection. Detachment at the stem-branch connection is unfavorable as fruit will be harvested with an attached stem. Harvested stems can cause damage to other fruit by puncturing, but also represent an extra process required to remove stems prior to export.

To better understand the forces required for detachment, a kiwifruit detachment jig was designed so that average detachment forces could be determined in relation to rotation angle (Fig. 4.8). The axial force required for detachment was measured for 60 kiwifruit across three different rotation angles. Table 4.1 shows that there is a factor of 7 difference between the mean forces from the 0° and 90° rotation

Rotation angle (°)	Mean force (N)	SD force (N)	Stems harvested
0	37.4	6.8	25%
45	14.7	5.1	0%
90	4.5	1.5	0%

Table 4.1: Detachment force (mean and standard deviation) and percentage of stems harvested across 60 kiwifruit at three different rotation angles

Figure 4.8: Testing out the forces required to detach fruit from canopy at different angles with force testing jig

trials. As expected, the stem was also detached 25% of the time when detachment was along the stem-axis (0°).

Important considerations when designing an optimal end-effector for fruit harvesting are the variance in fruit size, variance in end-effector location and fruit clustering. As an example, for a kiwifruit mean diameter D_{mean}, diameter variance $\pm\delta D_{mean}$, and locational variance of $\pm\sigma$ in the revelant plane; the end-effector design must accomodate for a minimum diameter D_{min}, where $D_{min} = D_{mean} + \delta D_{mean} + \sigma$. If harvesting a smaller sized fruit of diameter $D_{small} = D_{mean} - \delta D_{mean}$ within a tightly packed cluster, the end-effector can knock into neighbouring small fruit even with the most slender profile due to the larger diameter that it must accomodate. Thus, fruit size and location variance is conducive to an increased drop rate because of end-effector protrusion into neighbouring clustered fruit. The detachment process itself also causes clustered fruit to be knocked as the fruit is rotated. Therefore, it can be expected that neighbouring fruit will be knocked to some degree during the detachment process; it is beneficial for the end-effector to be as unintrusive as

possible during this process to minimize fruit damage.

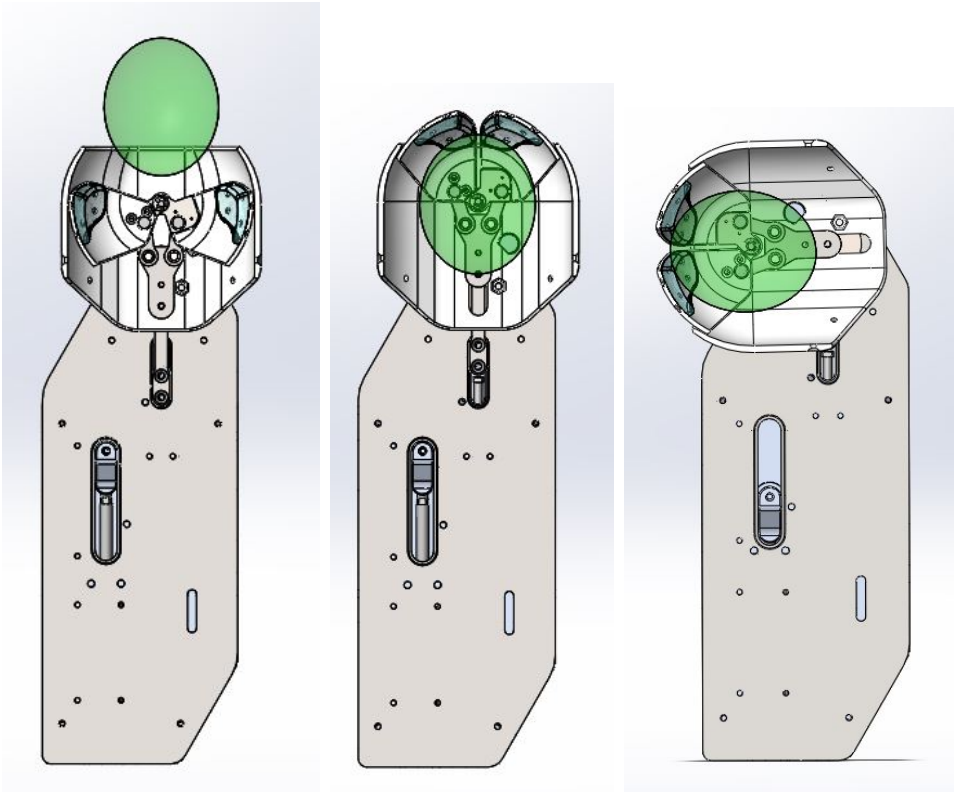

(a) Phase 1 (b) Phase 2 (c) Phase 3

Figure 4.9: Centered cross section of LHR end-effector showing three phases of detachment with a mean average sized New Zealand kiwifruit

The LHR end-effector design consists of a plastic sheath with a slightly conical upper edge and a beak-like shutter which acts as a 'go/no-go'. Once the kiwifruit is enveloped by the sheath, the beak shutter actuates closed; ensuring that fruit cannot be dropped once inside the sheath. Once the shutter is closed, the end-effector assembly rotates with fruit inside and the manipulator can then retract the end-effector downwards. These three phases are illustrated in Fig. 4.9. If the fruit is not detached by way of rotation alone, the rotation angle will mean that when pulled downwards the shear stress at the stem-fruit connection will cause detachment. The beak-shutter has low durometer silicone on the insides which contact fruit meaning that fruit will not be damaged as it is detached. Potential benefits to this design:

- A rounded and unintrusive profile which may help to reduce the knocking of neighbouring fruit from protrusion
- Does not require any physical gripping i.e. no side load on fruit

- The beak-shutter means that once inside the sheath, the kiwifruit are encapsulated and cannot be inadvertently dropped by the retraction of mechanism
- Compact actuation mechanism

Potential downsides/limitations to the design:

- If the vertical (Z axis) locational accuracy is poor, the beak-shutter could close part way up a fruit - potentially causing fruit damage
- The sheath may be prone to damage if forced against rigid obstructions in the canopy
- The rotation phase of the fruit may not be as effective as with a gripper due to less constraint

A push-rod mechanism was used for the beak-shutter, whereby a 10mm diameter pneumatic micro cylinder produced a symmetric torque for each side of the beak. A larger 16mm diameter cylinder was used for the rotation phase which used a small stainless steel cable and spring return, it was important to ensure the rotational force at the stem-fruit connection was sufficient to cause detachment as per Tab. 4.1. A challenge was to ensure that the push-rod actuation cylinder could remain static during rotation. To achieve this, a dynamic pivot was introduced in the push-rod mechanism such that the pivot aligned with the centre of rotation during the rotation phase. This meant there was less bulk to be rotated, further minimizing protrusion into neighbouring fruit, furthermore, because the mechanism pivot was locked into the centre of rotation the beak remained locked shut despite zero torque component provided from the 10mm cylinder. However, this could also be seen as a disadvantage if beak actuation was needed during the rotation phase.

The prototype sheaths and beaks of the LHR end-effector were 3D printed. It is forecast that due to the complex geometry, the 3D printing costs involved with manufacturing several hundred units may be reasonable in comparison to expensive injection mold tooling. A different 3D print material was used for each end-effector on the LHR with the objective of testing component performance in parallel with the concept itself. The two materials used were SLA (stereolithography) Somos 9120 resin, and MJF (multi jet fusion) nylon. These materials were chosen because of their strength, ductility (with high a percentage elongation before yield) and also accurate $\leq \pm 0.2mm$ print tolerances. Figure 4.10 shows the black, MFJ nylon version LHR end-effector being trialled in lab whilst mounted on the original KHM robot-arm.

To summarize, a novel end-effector was developed in an effort to reduce fruit damage by minimizing protrusion with an uninstrusive sheath design which also encapsulates fruit to prevent inadvertent dropping. A detachment force experiment was done to better understand the forces required to detach kiwifruit at different angles of rotation; this dictated the forces required of the end-effector rotation phase. Two end-effectors were built - one for each LHR robot-arm, each end-effector was made from a different material to test component performance in parallel with the concept itself.

Figure 4.10: In-lab testing of LHR end-effector concept mounted on KHM robot-arm

4.2 Control strategy

4.2.1 Architecture

From a systems perspective, the LHR is centralized around an 8 axis motion controller (Galil DMC-4183), Fig. 4.11.

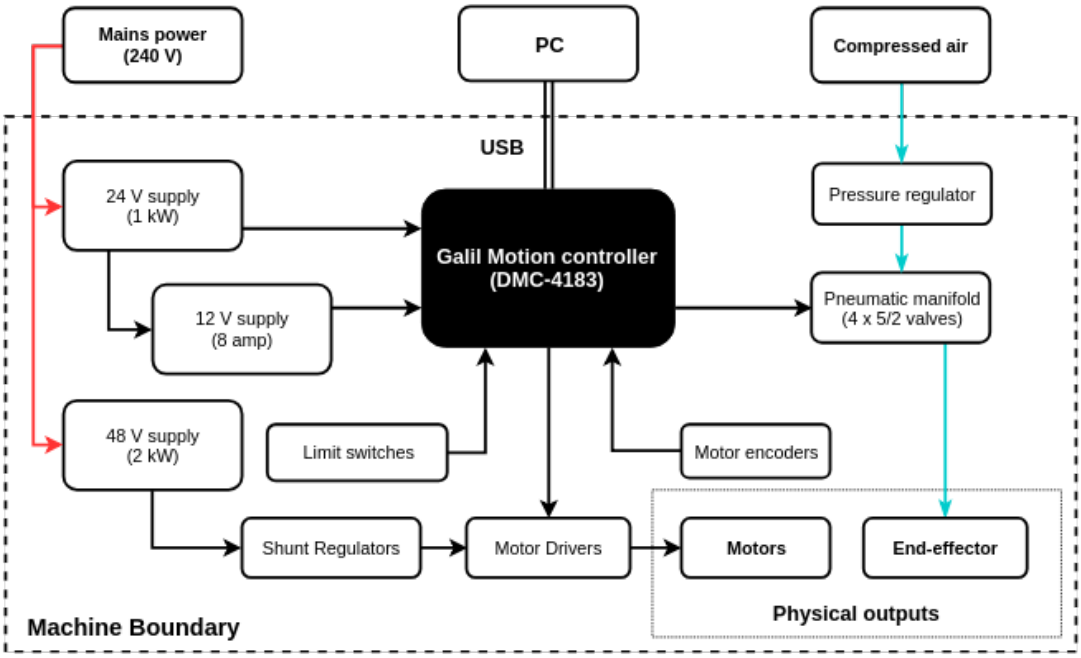

Figure 4.11: Simplified system architecture of the LHR robot

This motion controller has an array of features that made it an appropriate selection:

- Supports 8 axis motion control and multi-thread execution
- Custom application programming, Python and Linux API's
- Flash EEPROM for program and array storage
- Supports encoder feedback for position error handling
- Opto-isolated digital outputs for variable voltages and 500 mA source capacity (able to drive solenoids)
- USB connectivity

All interfacing with the controller, such as sending commands/programs etc. was done from a PC with an ASCII interpreted language specific to Galil

controllers called "DMC code". The back-end programs on the PC side were written with Python in the Linux operating system. Python was used due to its high-level functionality and large range of supporting modules, packages and libraries which enabled fast and relatively seamless development. The Python wrapper "gclib.py", provided access to the Galil "gclib" library of C functions as a programming interface with the controller.

4.2.2 Motion optimization and path planning

A key performance indicator of the LHR was the sub-phase time of moving from fruit to fruit when harvesting - this section will describe efforts taken to reduce and optimize this time from a software perspective. The point-to-point type move is the most common type of motion profile and often in high performance linear systems the velocity is the limiting parameter. Thus, motion will require a trapezoidal velocity profile with three phases; an acceleration phase, a maximum velocity phase and a deceleration phase. With other variables known, the time taken to finish a trapezoidal move can be derived from the velocity and distance relationship:

$$d = \int_0^t v(t)dt$$

$$d = \frac{v_{max}t_a}{2} + v_{max}t_c + \frac{v_{max}t_d}{2}$$

Assuming the profile is symmetric with equal acceleration and deceleration;

$$t_{trap} = \frac{d}{v_{max}} + \frac{v_{max}}{a} \tag{4.13}$$

Equation 4.13 states that the total time to complete the trapezoidal move is equal to the time taken to cover the distance at maximum velocity plus the time taken to reach maximum velocity. However, when velocity is not a limiting factor, the optimum point-to-point motion profile is a simple triangular move with an acceleration phase and a deceleration phase. Again assuming the profile is symmetric with equal acceleration and deceleration:

$$t_{tri} = 2\sqrt{\frac{d}{a}} \tag{4.14}$$

Velocity and acceleration are linear motion variables applicable to the drive in Eq. 4.13 and 4.14, the goal is to optimize these variables given a set of drive characteristics, inertia's and axis loading's. Stepper motors provide the linear motion on the LHR, consequently the maximum torque available on each axis of the LHR decreases with increasing motor speed.

To begin the optimization process, the torque vs angular velocity data for the X and T axis motors were approximated as third order polynomial curves Fig. 4.12b. Subsequently, a third order force function (F_{max}) with respect to linear velocity was obtained. The values of $F_{max}(v)$ are shown in Tab. 4.2. With the

Axis	$F_{max}(v)$
X	$-244.5v^3 + 1124v^2 - 1775v + 1083$
T	$-0.082v^3 + 2.954v^2 - 31.84v + 125.2$

Table 4.2: Polynomial approximations of maximum force with respect to velocity for both X and T axis

inclusion of a safety factor (SF), the forces for each X axis motor can be expressed:

$$F_{max}(v) = SF\left[\frac{m}{2}a(v)_x + \frac{\mu_f mg}{2} + a(v)_x\gamma\right]$$

Solving for acceleration with respect to velocity:

$$a(v)_x = \frac{F_{max}(v)}{SF(\frac{m}{2}+\gamma)} - \frac{\mu_f mg}{m+2\gamma} = -7.67v^3 + 35.3v^2 - 55.7v - 33.5 \tag{4.15}$$

There will exist a point on this 3rd order linear acceleration curve which will provide an optimum time solution for a given travel distance. Therefore, when substituting the X-axis acceleration function into the trapezoidal time expression:

$$t_{trap} = \frac{d}{v} + \frac{v}{-7.67v^3 + 35.3v^2 - 55.7v - 33.5} \tag{4.16}$$

And for triangular motion:

$$t_{tri} = 2\sqrt{\frac{d}{-7.67v^3 + 35.3v^2 - 55.7v - 33.5}} \tag{4.17}$$

The point at which these two expressions converge is the triangular transition point and represents the velocity at which the trapezoidal model breaks down with increasing velocity due to the absence of a maximum velocity phase. Similarly, the triangular model breaks down with decreasing velocity from this point due to the presence of a maximum velocity phase. This point occurs when half the total distance is travelled during a single phase of motion:

$$\frac{d}{2} = \frac{v^2}{2a(v)_x}$$

Rearranging and substituting for the X-axis acceleration:

$$\frac{v^2}{-7.67v^3 + 35.3v^2 - 55.7v - 33.5} - d = 0 \tag{4.18}$$

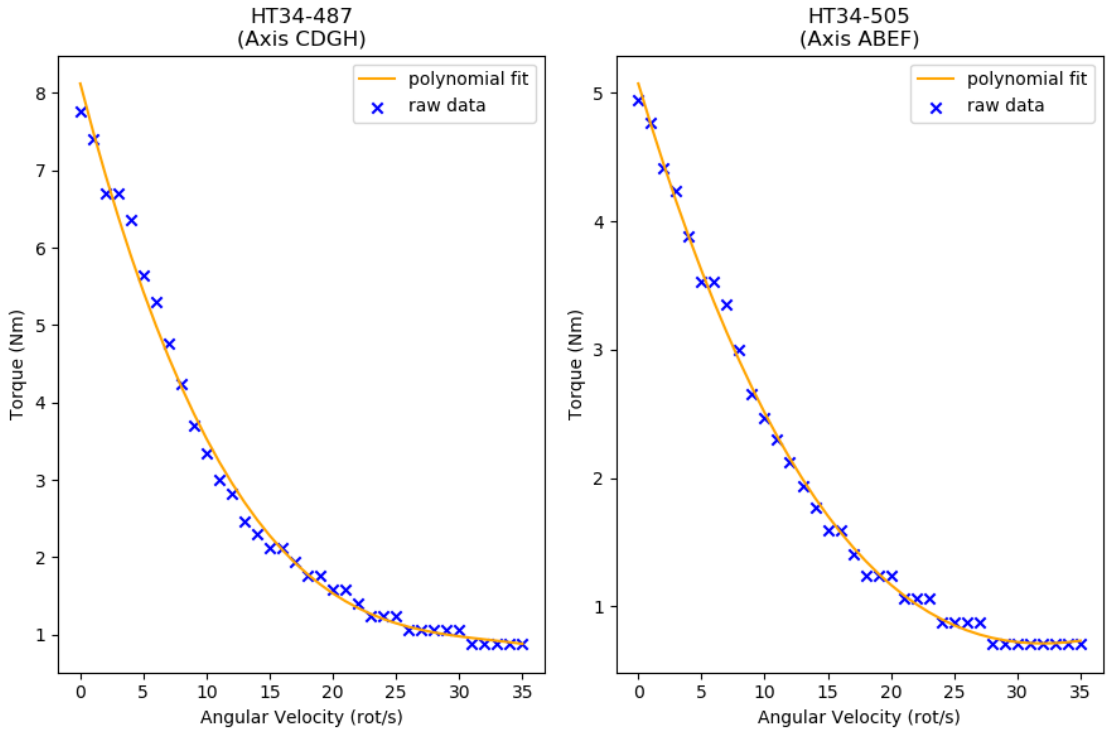

(a) LHR polynomial fitted torque vs speed data for X (HT34-487) and T (HT34-505) axis motors

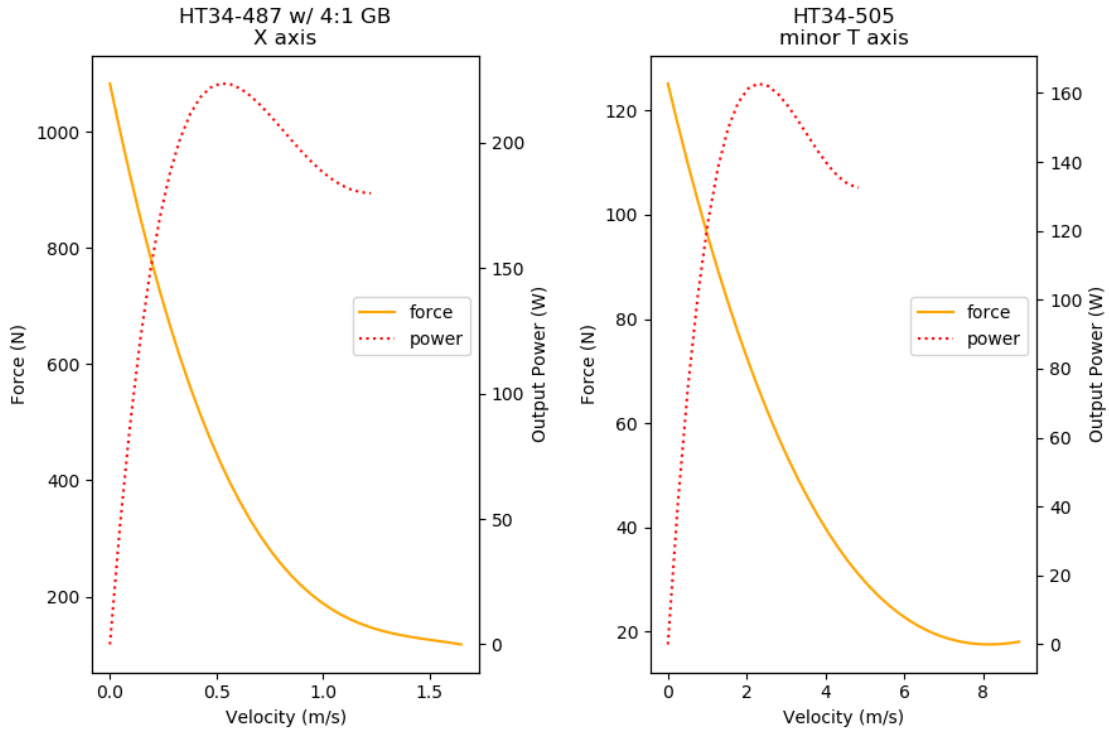

(b) LHR polynomial fitted linear accleration and power outputs

Figure 4.12: LHR drive properties

Where the value of velocity (v) in Eq. 4.18 is equal to the triangular transition velocity and was solved using the Newton–Raphson method [63]. Maximum velocities reached above this triangular transition velocity are not indicative of the drive limitations and are defined by the acceleration and time. Thus, any solution above the triangular transition velocity will be sub-optimal. A minimal solution for the non-linear time expression for trapezoidal motion in Eq. 4.16 was solved using the Nelder-Mead simplex algorithm [64].

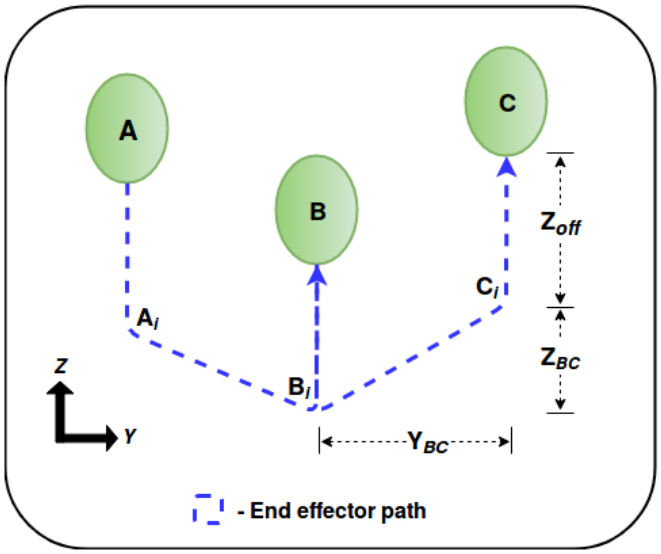

Figure 4.13: A picking scenario showing the motion path taken by the end effector

A more rigorous approach is required to optimize the T-axis drives. Figure 4.13 shows the approximate path required of the end-effector travel in the YZ plane. Fruit must be approached and departed in exclusively Z axis motion to reduce the chance of knocking neighbouring fruit and to ensure the detached fruit enters the end-effector as intended. Therefore, a path between fruit will consist of three stages; a Z axis retraction stage (Fruit A to point A_i), a multi-axis motion stage to new fruit location (A_i to B_i) and a Z axis extension stage (B_i to fruit B). Scarfe and Williams et al. proposed the merging of these phases into a U-move profile to decrease time [6][59]. Stages one and three are straight-forward to solve for during T axis optimization as both motors are contributing in even amounts with obvious loading in the Z axis. Stage two is more difficult to solve for because each motor will have different loadings depending on the net change in position:

$$\Delta\theta_{T_1} = \Big[-\Delta Y\beta + \Delta Z\beta \Big] \qquad \Delta\theta_{T_2} = \Big[\Delta Y\beta + \Delta Z\beta \Big]$$

Another stage two requirement is that, for a given net position change, the motor with the lesser magnitude T vector has a velocity component equal to

or less than the larger magnitude T vector. This ensures that the actual motion trajectory produces displacement within bounds that will not cause collision with the kiwifruit and/or hard limit stops of the machine. Therefore, a sub-optimal but less problematic time solution is to assume a maximum loading scenario and that the accelerations and velocity profiles for each T motor are identical and solved for the motor with the greater magnitude T vector.

$$a(v)_{T_1} = a(v)_{T_2} \qquad [\, a_{T1\ opt}, v_{T1\ opt} = a_{T2\ opt}, v_{T2\ opt} \,]$$

With the inclusion of a safety factor, the forces for each linear T axis can be expressed:

$$F_{max}(v) = SF\Big[\mu_f m_y g + m_z g + a(v)_T(m_y + m_z)\Big]$$

Solving for acceleration with respect to velocity:

$$a(v)_T = \frac{F_{max}(v)}{SF(m_y + m_z)} - \frac{g(\mu_f m_y - m_z)}{(m_y + m_z)} = -0.013v^3 + 0.46v^2 - 4.91v - 29.9 \quad (4.19)$$

In summary, this optimization method for trapezoidal and triangular motion can be used in conjuction with fruit scheduling algorithms, such that an optimum time solution can be approached for a specificed distance between points. Keeping motor characteristics constant, updates to optimum velocity and acceleration values on a per distance basis can be input into a controller with a modest time complexity.

4.2.3 Fruit scheduling

Cluster management and registery allocation

Instead of being homogeneously spaced, kiwifruit typically grow in clusters. In some cases these clusters can be relatively dense. Clustered fruit are difficult to pick robotically as the end-effector will tend to knock neighbouring fruit when picking due to localization inaccuracy and end-effector protrusion (Section 4.1.2). This can cause fruit damage and/or cause fruit to detatch from their stem and fall to the ground. As mentioned prior (Sections 3.2), fruit damaged or dropped are considered rejects and thus attribute a profit loss to the orchard owner. It may be unrealistic to expect a system capable of zero interaction with neighbouring fruit, but with an unobtrusive end-effector and correct picking order - a large portion of 'neighbour knocking' can be minimized. Scarfe [6] and Williams et. al [59] proposed methods of scheduling kiwifruit on a per cluster basis, see Fig. 4.14. Albeit different in

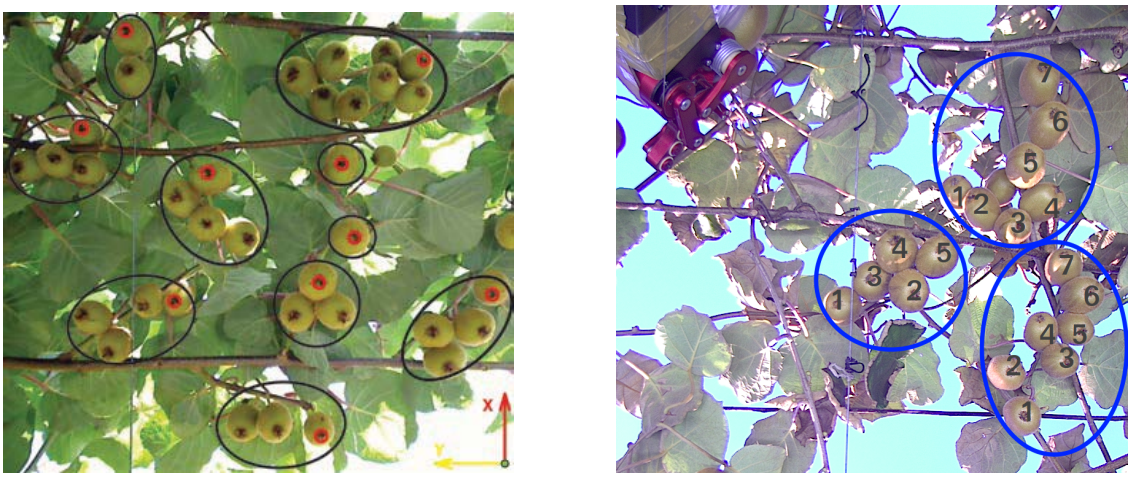

(a) Scarfe kiwifruit cluster scheduling

(b) Williams kiwifruit cluster scheduling

Figure 4.14: Prior kiwifruit cluster scheduling methods

specifics, Scarfe and Williams methods both involve cluster-classification based on grouping, and then schedule the fruit within those clusters such as to minimize the chance of fruit damage. Clusters allocated to arms are then picked in a way that minimizes the chances of arm collision. A similar but slightly different approach was taken towards scheduling and cluster management on the LHR. Fruit locations were added to the register of arms from a global workspace with two classifiers. The first classifier - a cluster management rule wereby clusters were not explicitly identified, but a fruit could not be added to a register if it was dependent on another fruit being picked first. A fruit has dependencies if another fruit is lower and within some pre-defined XY planar distance to avoid end-effector collision. The second classifier - a scheduling method for prioritizing the next fruit if the first classifier is not valid. Two types of scheduling method were developed for the LHR, 'x rank' and 'greedy'. Figure 4.15 demonstrates the scheduling process on the LHR with flow-chart showing the registry allocation process. On the LHR, the end-effector rotation is from left-to-right and is required for stemless detachment of fruit (section 4.1.2), but can cause damage to other clustered fruit in the rotation process. To minimize this, it is preferable to approach fruit in the opposite direction to the rotation - this was noted by both Scarfe and Williams.

To approach the fruit from the right, the arms on the LHR will need to have their register initialized on the right-side of their workspace (not always the case with 'greedy'). However, initial fruit may have dependencies further to their right which will cause the arms to enter into the workspace of the right-side arm. Discrepencies in the distribution of work between arms can be minimized in this case, if the arm registers are prioritized sequentially along the x-axis. If kept sequential,

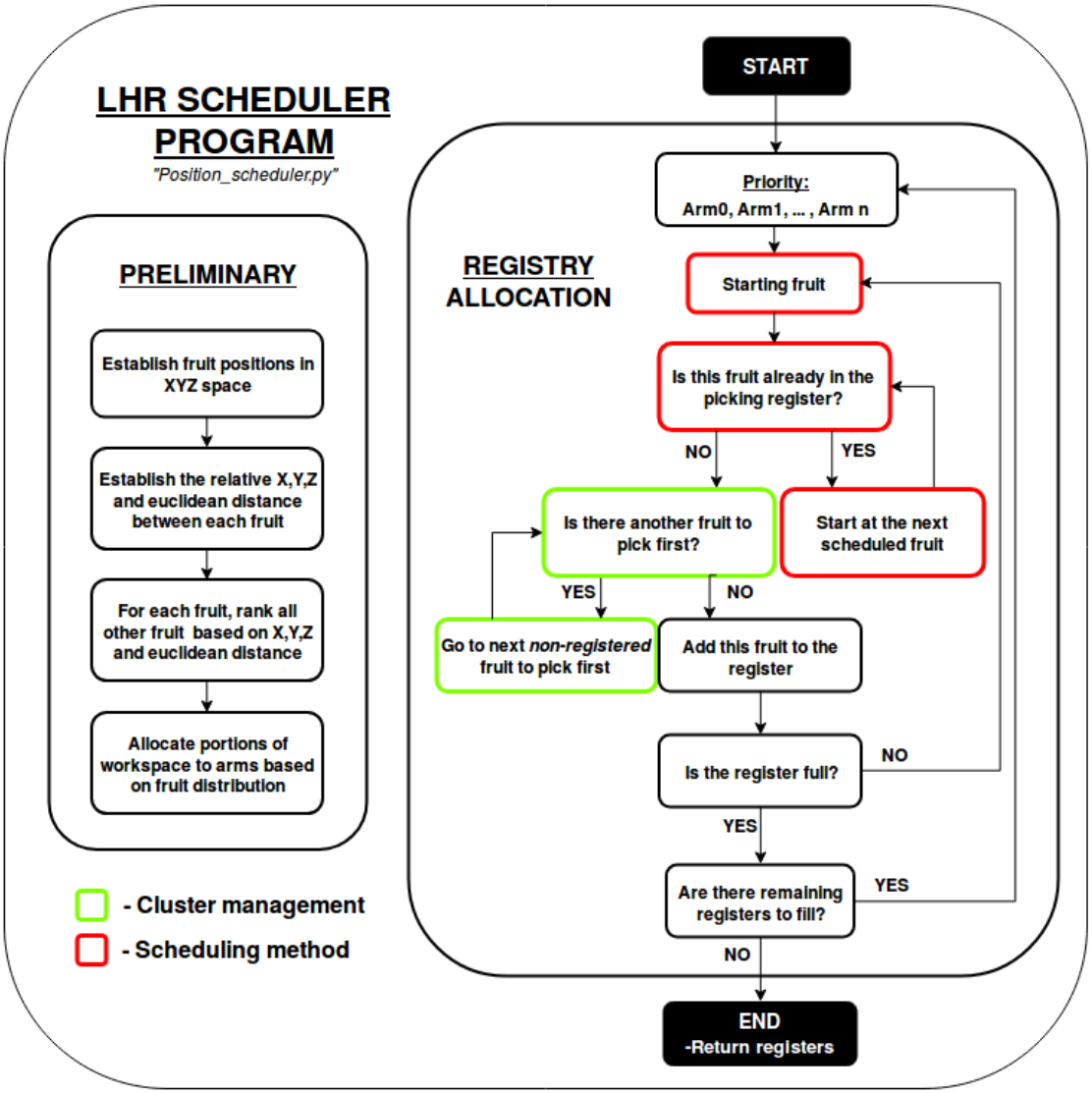

Figure 4.15: A high-level diagram of the LHR scheduler with registry allocation flow-chart

arm2 could lose fruit to arm1 to its left but could take fruit from arm3 to its right in the case of dependencies, and so forth up until the N^{th} arm in an N arm system (which may have some compromised parity in work as it cant take fruit from another workspace). If the registers are non-sequential along the x-axis, some of the fruit which could of typically been picked by arm2 has been picked by arm1 to the left *and* arm3 to the right. Thus, in the interest of maintaining work parity and reducing fruit rejects; arm workspaces should be initialized on the right-side and prioritized sequentially along the x axis from left to right.

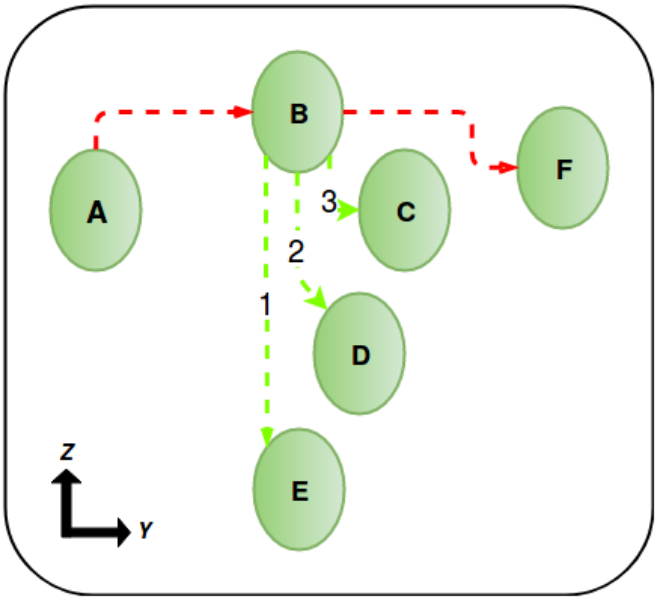

Figure 4.16: A clustered-kiwifruit picking scenario handled with the proposed LHR 'x rank' algorithm

'x rank'

'x rank' is a simple scheduling method that dictates that the next fruit in the picking register will be the closest fruit in the X-axis direction, unless the cluster management routine intervenes. The premise behind 'x rank' is that the linear axis arms will generally only ever travel in one direction during a static harvesting cycle. The perceieved benefits to this method are that the arms can travel in the opposite direction to the end-effector 'snapping' motion; reducing risk of fruit rejects. There is a also a reduced risk of the arms colliding with each other as they are all travelling in the same direction with an equal work distribution. The downside to this method is that the fruit-to-fruit cycle times may be relatively large due to large Y-axis distance between sequentially registered fruit. Figure 4.16 displays how the algorithm works when combined with cluster management. The 'x rank' algorithm takes the following process:

- Start at Fruit A. Fruit A has no dependencies; fruit A added to register
- Fruit B is the next 'x-ranked' fruit from A, however, it is dependent on fruit E, D and C being picked first
- Fruit E is the lowest in this dependent group and has no dependencies of its own; fruit E added to register
- Fruit D is next-lowest valid dependency of B. Fruit D is dependent on fruit E, but fruit E is already in register, thus fruit D has no valid dependencies of its

	Dependencies
A	none
B	E, D, C
C	E, D
D	E
E	none
F	none

(a) Ordered dependencies

1^{st}	2^{nd}	3^{rd}	4^{th}	5^{th}	6^{th}
A	E	D	C	B	F

(b) Ordered register

Table 4.3: Outcomes from picking scenario with 'x-rank' as shown in Fig. 4.16

own; fruit D added to register

- Fruit C is next-lowest valid dependency of B; fruit C is dependent on D and E thus has no valid dependencies of its own; fruit C added to register
- Fruit B has no valid dependencies; fruit B added to register
- Fruit F is the next 'x-ranked' fruit from B and has no dependencies; fruit F added to register
- No more fruit available for scheduling; register finished

For each allocation in an arm's register, 'x rank' will start at the same initial fruit location and loop through until a valid fruit location is found. Therefore, if a scheduled fruit has dependencies, all dependencies (and potentially sub-dependencies) will be scheduled first - followed by the originally scheduled fruit. Thus, the 'x rank' solution is bound by dependency-tree's which it will pick through in order, shown in Fig. 4.16.

'greedy'

'greedy' is a heuristic solution to the 'travelling salesmen problem'. It dictates that the next fruit in the picking register will be the closest fruit in three-dimensional euclidean distance, unless the cluster management rule intervenes. The premise behind 'greedy' is that the LHR end-effectors will follow a semi-optimal path to decrease sub-phase time between fruit. Nearest neighbour (NN) and greedy algorithms are typically capable of producing a travelling salesman solution that is, on

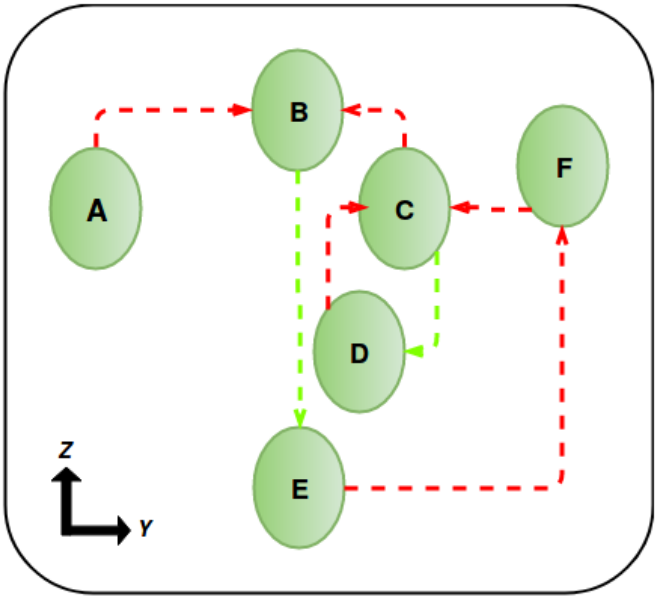

Figure 4.17: A clustered-kiwifruit picking scenario handled with the proposed LHR 'greedy' algorithm

average, within 25% of the Held-Karp lower bound[65]. Despite the potential time gains, the direction of x-axis travel is variable and only depends on where the next closest fruit is. As a result, there is an increased risk for both fruit rejection and arm collison. Figure 4.17 displays how the algorithm works when combined with cluster management. The 'greedy' algorithm takes the following process:

- Start at Fruit A. Fruit A has no dependencies; fruit A added to register
- Fruit B is the next 'greedy' fruit from A, however, it is dependent on fruit E, D and C being picked first
- Fruit E is the only non-dependent fruit from fruit B's dependency group; fruit E added to register
- Fruit F is the next 'greedy' fruit from E. Fruit F has no dependencies; fruit F added to register
- Fruit C is the next 'greedy' fruit from F. Fruit C is dependent on fruit E and D. Fruit E is not valid as is already in register. Fruit D is next lowest in dependent group with no valid dependencies of its own; fruit D added to register
- Fruit C is the next 'greedy' fruit from D. Fruit C has no valid dependencies; fruit C added to register
- Fruit B is the next 'greedy' fruit to be detached. Fruit B has no valid dependencies; fruit B added to register
- No more fruit available for scheduling; register finished

	Dependencies
A	none
B	E, D, C
C	E, D
D	E
E	none
F	none

(a) Ordered dependencies

1^{st}	2^{nd}	3^{rd}	4^{th}	5^{th}	6^{th}
A	E	F	D	C	B

(b) Ordered register

Table 4.4: Outcomes from picking scenario with 'greedy' as shown in Fig. 4.17

Unlike 'x rank', for each allocation in an arm's register, 'greedy' will start at the previously scheduled position in the register. Consequently, if a scheduled fruit has dependencies, the lowest non-dependent fruit will be scheduled first - followed by the next 'greedy' option from the perspective of that non-dependent fruit. Thus, the 'greedy' solution is not bound by any dependency-tree, seen in Fig. 4.17.

Chapter 5

Evaluation and Discussion

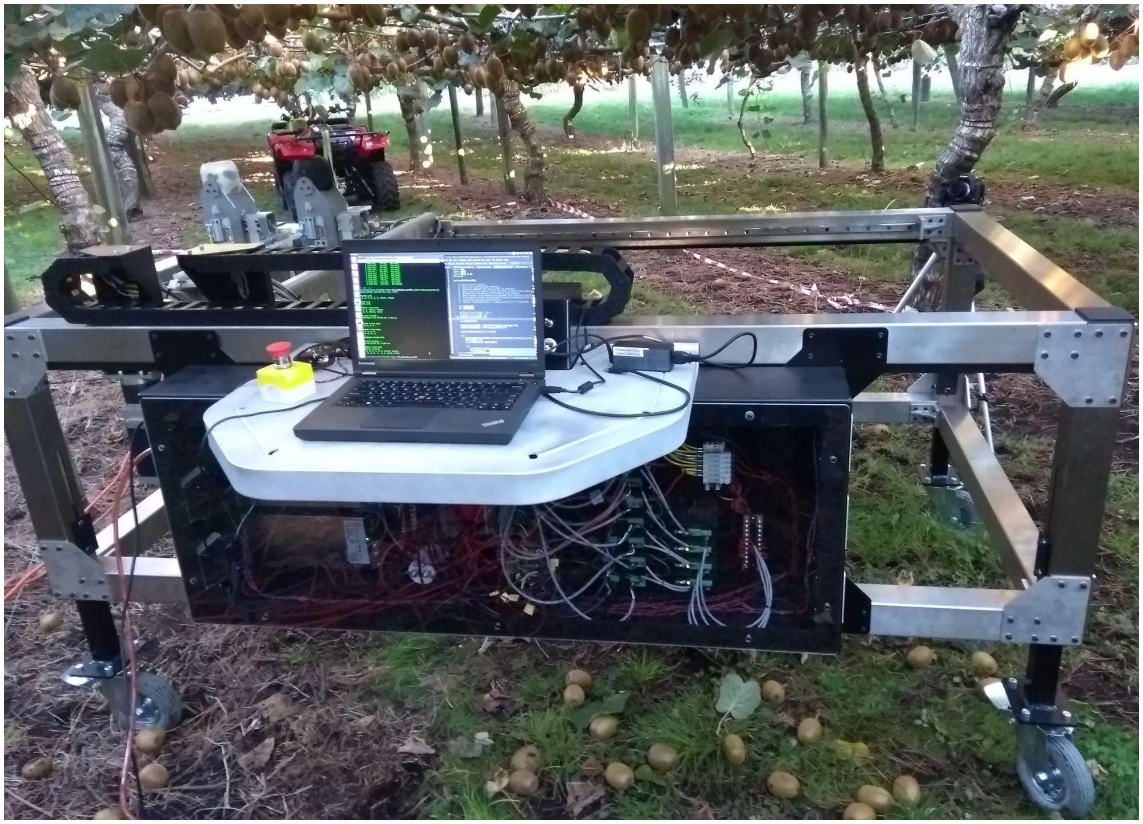

Figure 5.1: LHR robot testing in kiwifruit orchard

The research aim was to establish whether a prismatic axis kinematic structure was more effective than a rotational axis kinematic structure, for the multiple-robot harvesting of kiwifruit. A prismatic axis kiwifruit robot (LHR) was developed, built and tested. LHR kiwifruit harvesting performance was evaluated over 10 phases of static workspace; five from the Batemans orchard and five from the Newnham orchard. Both orchards grow Hayward strain kiwifruit with a pergola style located in Tauranga, New Zealand.

5.1 Harvest cycle time

5.1.1 Work distribution and scalability

		Orchard region									
		1	**2**	**3**	**4**	**5**	**6**	**7**	**8**	**9**	**10**
$\mathbf{W_D}$	**LHR 'xrank'**	1	0.98	0.93	0.88	0.94	0.93	0.97	0.94	0.84	0.97
	LHR 'greedy'	1	0.98	0.93	0.88	0.94	0.93	0.97	1	*	0.97
	KHM (A)	0.93	0.93	0.53	0.50	0.66	0.51	0.60	0.54	0.86	0.48
	KHM (B)	0.65	0.63	0.88	0.67	0.79	0.60	0.54	0.62	0.93	0.53

All regions		
$\mathbf{W_D}$	**LHR 'xrank'**	0.94
	LHR 'greedy'	0.95
	KHM (A)	0.64
	KHM (B)	0.71

Table 5.1: Mean average Work distribution constant W_D across 10 recorded regions of kiwifruit orchard canopy. (* = unavoidable collision)

Work distribution was measured using the proposed Work distribution constant W_D defined in Eq. 3.3 as the work done by each robot-arm at parity over the busiest robot arm. Values are shown in Tab. 5.1.

The fruit registery was recorded for each LHR robot-arm within each orchard region using the 'x-rank' algorithm. This process was then repeated in-lab with recorded fruit positions for each orchard region using the 'greedy' algorithm. The mean average W_D value was 0.95 and 0.94 across all regions for 'greedy' and 'x-rank' respectively. This meant that the work done by the busiest robot arm was, on average, within 6% of an ideal parity work distribution. Limitations to achieving parity ($W_D = 1$) were due to the total number of fruit not perfectly divisible by the

number of robot arms, but of more significance was the effect of fruit dependencies due to the cluster management software. During 8 out of 10 of the orchard regions, W_D was identical for both 'x-rank' and 'greedy'. The predominant outlier is orchard region 9 where a cluster management dependency tree at the workspace-split caused the 'x-rank' W_D value to drop two standard deviations below the mean. The 'greedy' algorithm was unable to progress through orchard region 9 without collision between robot-arms, this was the case despite efforts to adjust the workspace split location.

An attempt was made to evaluate KHM work distribution on the same orchard regions and fruit positions recorded by the LHR. A limiting factor to this evaluation is that the workspaces of the LHR and KHM have workspace regions which exist as no subset of the other's workspace. To account for this, it was assumed that the KHM robot-arms were able to pick all fruit recorded by the LHR such that the only metric conducive to the W_D value was the X axis restriction on each RRR robot arm. Hence, the LHR recorded fruit positions were centrally imposed on a virtual KHM workspace and each KHM robot-arm was allocated fruit positions based on X axis value. The X axis span of LHR recorded fruit positions entirely covered the two inner robot-arms of the KHM but only partially covered the workspace of the two outter robot-arms. To adjust for discrepency in the X axis span, one method used (method A) was to scale the effective work distribution of the outter arms based on the X axis coverage. Another approach (method B) was to scale the entire LHR workspace such that all recorded fruit positions were distributed entirely across the KHM robot-arms. Both of the afforementioned methods are, to different degrees, analogous to the assumption that the heterogenity of a subset of the orchard canopy is representative of a larger region which is non-ideal.

Seperate regions		
$\mathbf{W_D}$	**LHR 'xrank'**	0.94
	KHM (C)	0.5

Table 5.2: Work distribution constant W_D for KHM (method C) and LHR 'x-rank' across seperate regions

In section 2.2.2, it was found that the average maximum discrepancy in work distribution between the most active and least active robot-arm was 52.3% across 3 orchards, 39 trial regions and 698 fruit. From this same data, the mean

Work distribution constant across these regions (method C) was calculated as part of this study to be $W_D = 0.5$. Despite the use of different orchard regions to those evaluated on by the LHR, method C is a statistically superior measure of KHM W_D value than the other methods and issues no inference regarding workspace intersection. A weakness to this evaluation remains despite the adoption of method C, in that there is an inherent assumption that the heterogenity of fruit is comparable between orchard regions. It is currently unknown how many trial regions and/or seperate orchards of testing are required to achieve a conclusive W_D value.

A scenario which amplifys fruit heterogenity across a workspace is when the orchard row width is not perfectly divisible by the workspace width so that some fraction of the orchard row remains to be harvested. If the canopy taskspace spans only half of the KHM workspace; two of the robot-arms will do nothing - decreasing the W_D value. The LHR was tested in-lab on a group of 20 artificially created fruit positions which spanned full workspace, half workspace and the equivalent of a single KHM robot-arm workspace. The LHR maintained a mean W_D value of 0.94 throughout these artificial regions whilst using the 'x-rank' algorithm and 0.92 using 'greedy'. This was possible as the robot-arms on the LHR have an effective workspace which is some fraction of the overall workspace; dictated by the taskspace intersection and requirement of work.

Of note is the result that 'greedy' performed slightly worse than 'x-rank' with the artificially generated positions despite performing slightly better on the real orchard positions, the reason is partially due to robot-arm collision. Collision on the LHR occurs due to the physical width of a robot-arm comprising a portion of another robot-arm's workspace. This happens less frequently with 'x-rank' as all robot-arms are generally travelling in the same X axis direction and will consistently finish their task at a certain side of their workspace. Whereas 'greedy' is free to find a solution that can potentially back-track on itself. Figures 5.2 and 5.3 graphically display the order of fruit within arm0 (blue line) and arm1 (red line) for 'x-rank' and 'greedy'. The lower mean W_D value for artificially generated positions is due to the alteration of the workspace split location (also termed 'x-break'); effectively moving the 'line in the sand' in an effort to promote a non-colliding path. Altering the workspace split meant that instead of a $\sim$50% allocation of fruit, the allocation was slightly bias towards one of the robot-arms in order to prevent a potential collision. This method was only partially successful and still resulted in unavoidable crash scenarios for 9 out of the 20 artificial regions for 'greedy' and 2 out of 20 for 'x-rank'. The implementation of collision prevention software should be a priority for any further iterations of the LHR.

The work distribution measure W_D is derived from the harvest cycle time equation (Eq. 3.2), which intrinsically assumes that the distribution of work is on average equivalent to the distribution of time. However, the introduction of collision prevention would likely introduce some degree of operational downtime despite the equal allocation of work. Scenarios prone to collision with 'x-rank' are when there is an increased density of operational robotic-arms per volume. A robot-arm density increase is present with the reduction of workspace (such as the afforementioned partial taskspace span across the workspace) or when there is an increase in robot-arms such an when scaling the system. Therefore, it can be inferred that LHR work distribution is a function of the number of robot-arms for a given workspace due to the operational downtime introduced to prevent collision.

The likelihood for collision can be reduced, and thus work distribution increased, by reducing the robot-arm width relative to the robot-arm effective workspace. The differential drive, rolling-element constrained design of the LHR robot-arm was seen as a method of achieving this (section 4.1.1) by reducing the value of γ (Eq. 4.4) and consequently the X axis carriage length. The resulting 2γ value on the LHR was less than 1% of the total arm mass, suggesting that there is room to further decrease carriage length without incurring any signicant reduction in drive efficiency. In justification of the LHR robot-arm design, for identical geometry but with plain-bearing motion constraint and 100% additional YZ carriage dynamic mass, the resultant 2γ value would of caused a 40% loss in X axis drive efficiency.

In summary, it was found that the LHR 'x-rank' mean W_D value is at minimum 88% greater than the mean W_D value of the KHM and that this percent disparity will increase as the workspace and taskspace intersection decrease. The LHR could operate both robot-arms within a single KHM robot-arm's X axis workspace span whilst achieving a maximum work distribution of $W_D = 0.95$. It was deduced that work distribution is a function of the number of robot-arms due to anti-collision downtime and that the LHR design promotes increased work distribution.

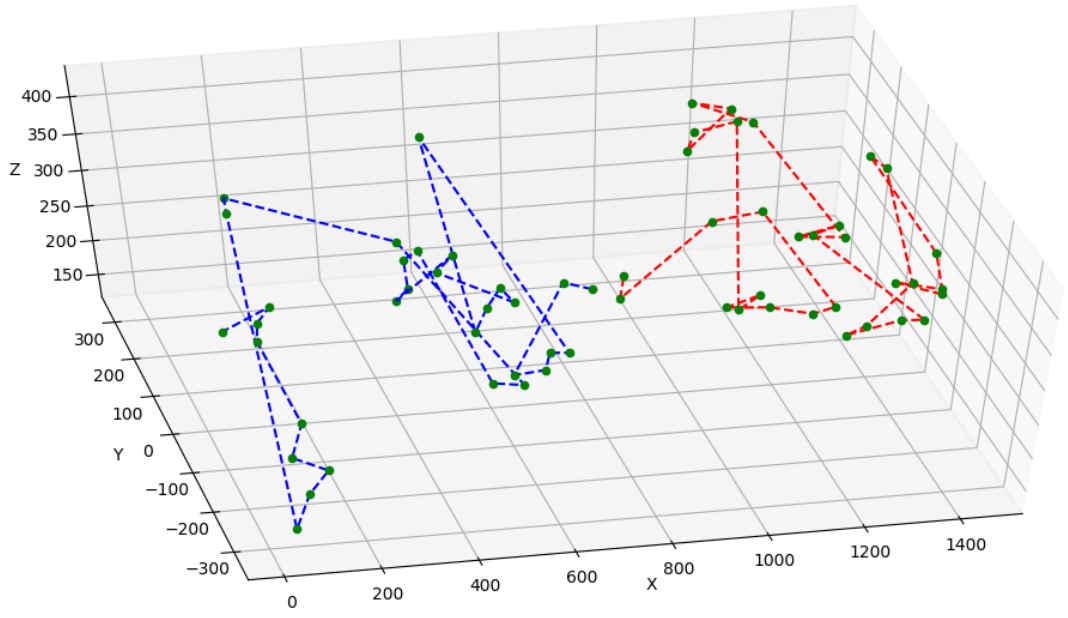

Figure 5.2: Fruit scheduling path by the 'xrank' algorithm for both LHR robot-arms on orchard region 1

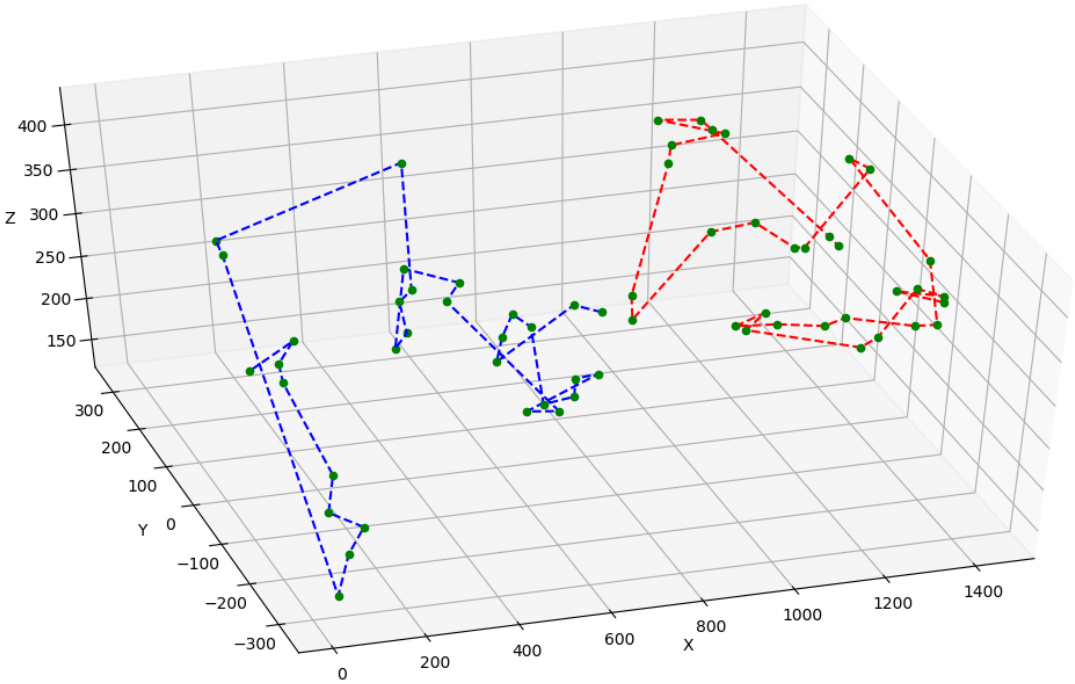

Figure 5.3: Fruit scheduling path by the 'greedy' algorithm for both LHR robot-arms on orchard region 1

5.1.2 Fruit per phase

	KHM			**LHR**		
	Total W-space	Phase Advance	Task Intersect	Total W-space	Phase Advance	Task Intersect
Volume (m^3)	1.12	0.42	0.3	0.44	0.44	0.42

Table 5.3: Workspace volume analysis of KHM and LHR

	KHM	**LHR**
Workspace efficiency (%)	26.9	95.2
Worst-case per arm efficiency (%)	16.2	95.2

Table 5.4: Workspace efficiency of KHM and LHR

Fruit per phase was deemed an important evaluation metric applicable to harvest cycle time and was defined as the harvestable taskspace volume per phase (V_h) in Section 3.2.1.

The orchard canopy taskspace volume was assumed to span 400mm in the vertical Z dimension; this includes 300mm of distributed kiwifruit and 100mm for extension and retraction of the end-effector as described in section 4.2.2. The X,Y task space dimensions were assumed to span the orchard row width and row length respectively.

The total workspace volume was calculated as the non-overlapping, combined volume of the robot-arms on each system. The upper approximation of this volume spanned $1.12m^3$ on the KHM, over 2.5 times greater than the LHR. The phase advanced volume accounted for the phase advance distance in the Y axis direction for each system. The KHM phase advance distance was limited at 300mm due to a non-isotropic workspace geometry, this led to a phase advanced volume of $0.42m^3$. The LHR phase advanced distance is equal to the Y axis stroke due to an isotropic workspace in the phase advance direction, consequently there is no change

between the phase advance volume and the workspace volume. The harvestable taskspace volume per phase (V_h, denoted Task Intersect in Tab. 5.3) accounts for the portion of phase advanced workspace responsible for performing work harvesting kiwifruit for any given phase. V_h on both systems was taken as the maximum volume component spanning 400mm in the vertical Z dimension. The LHR has a V_h value 40% greater than the KHM despite the KHM having a 150% greater total workspace which is reflected by the workspace efficiency in Tab. 5.4. The KHM worst-case per arm efficiency of 16.2% is a measure of the individual inner robot-arm V_h over the maximum individual RRR workspace of $0.402m^3$.

5.1.3 Sub phase time

		Orchard region									
		1	**2**	**3**	**4**	**5**	**6**	**7**	**8**	**9**	**10**
$\mathbf{t_{sp}}(s)$	**'xrank'**	1.85	1.84	1.86	1.85	1.85	1.89	1.87	1.85	1.85	1.85
	'greedy'	1.84	1.84	1.85	1.84	1.84	1.88	1.84	1.86	*	1.85
$\mathbf{d_f}(mm)$	**'xrank'**	67.1	63.6	78.1	54.0	63.9	78.5	78.0	61.6	68.9	60.7
	'greedy'	54.9	53.1	50.2	39.9	53.1	61.1	54.2	61.3	*	55.7

All regions		
$\mathbf{t_{sp}}(s)$	**'xrank'**	1.85
	'greedy'	1.85
$\mathbf{d_f}(mm)$	**'xrank'**	67.5
	'greedy'	53.7

Table 5.5: Sub-phase time t_{sp} and euclidean distance between sequentially registered fruit d_f across 10 recorded regions of kiwifruit orchard canopy. (* = unavoidable collision)

Sub-phase time was defined in Section 2.2.2 as the time taken between fruit within a harvesting phase and was an important metric within the harvest cycle time equation. On the LHR, this was inclusive of a $500ms$ end-effector actuation time, stage one time taken to retract the end-effector 100mm, stage two time taken to move to the next registered fruit location and stage three end-effector extension of 100mm. This was measured in-lab by the motion controller across all orchard regions and all fruit positions. A significant result from this section is that the mean sub-phase time for 'x-rank' and 'greedy' were almost identical within regions and across all regions depite a 26% greater euclidean distance between the sequentially registered fruit of 'x-rank' compared to 'greedy'. Figure's 5.2 and 5.3 show the plotted register allocation between fruit for both robot-arms using 'x-rank' and 'greedy' respectively.

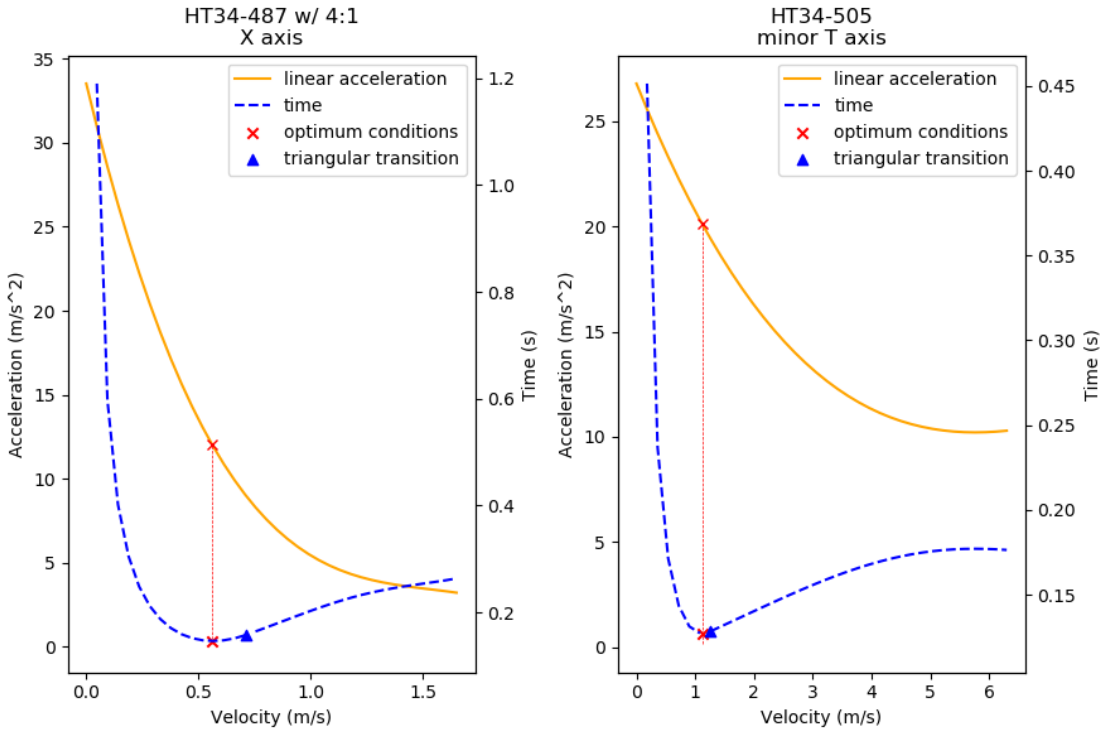

Figure 5.4: Motion time optimization output for X and T axis linear motion

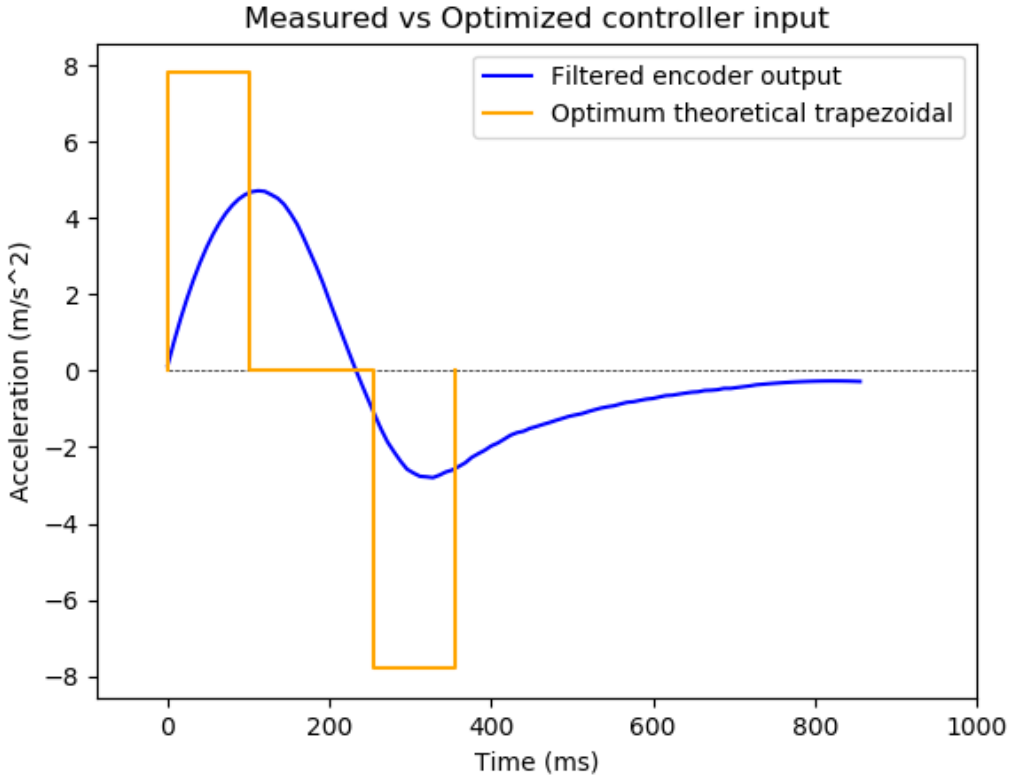

Figure 5.5: Comparison between optimized controller inputted acceleration vs the measured acceleration as a filtered encoder output for a 200mm X axis move

The optimization method proposed in Section 4.2.2 resulted in the output shown in Fig. 5.4 for an average 'x-rank' stage two move. The theoretical optimized sub-phase time result for a mean 'x-rank' move was $0.81s$; more than a full second less than the real result despite the motion controller receiving the optimized drive variables for velocity and acceleration. Fig 5.5 shows the difference between the optimized controller inputted acceleration and the measured encoder output for a 200mm X axis move. Detailed analysis into the sub-phase time optimization exist outside the scope of this report but the next reasonable step would be to alter the optimization model to include an 'S-curve' 3rd order component such as described in [66] to account for non-infinite jerk. The electrodynamics of the controller and drive may also contribute in non-trivial amounts as well as any anti-resonance compensation proportional to the drive inertia.

5.2 Harvestability and damaged fruit

	Orchard region									
	1	**2**	**3**	**4**	**5**	**6**	**7**	**8**	**9**	**10**
Number of fruit	62	51	28	35	47	26	31	34	52	35
Harvested (%)	81	80	93	57	72	54	87	76	81	86
Dropped (%)	16	0	7	14	15	19	13	18	8	11

All regions	
Total fruit registered	401
Harvested (%)	77
Dropped (%)	12

Table 5.6: LHR kiwifruit harvesting performance across 10 regions

Table 5.6 shows the LHR harvesting performance across the 10 regions of orchard taskspace. Of the fruit that were attempted, on average 80% were successfully harvested which was 77% of all fruit registered. This slight discrepency is due to a small number of false positive scheduled fruit and occasional failure of the end-effector rotation. This harvested percentage is not indicative of all fruit within the taskspace, only of fruit within the LHR workspace. An additional metric would have been to compare the registered fruit with all fruit within the orchard canopy for a comprehensive harvestability measure.

Figure 5.6: LHR robot-arms harvesting kiwifruit in orchard

The LHR end-effector was developed with the premise of reducing the kiwifruit drop rate with a non-intrusive profile. The LHR dropped and/or knocked 12% of attempted fruit, which is less than half of the drop/knock rate of the KHM during 2017. However, the 2018 KHM's revised end-effector and scheduling software combined to achieve an 8.8% drop rate in 2018; 27% less than the LHR and across a 30 times greater sample size. An attempt was made to compare the drop and harvest rates with the LHR manual localization and the KHM stereo vision localization. This was done by mounting the LHR end-effector on one of the four KHM robot arms whilst harvesting fruit in the orchard. Data collected for this scenario was ultimately deemed not suitable for comparison as the LHR end-effector was operating with different actuation characteristics. Also, the kinematic offset on the KHM with LHR end-effector had also not been validated which would of added more time constraint to the project. The two 3D printed materials (MJF nylon, Somos 9120 resin) used for the end-effector sheath and 'beak' profiles withstood the harvesting trials without any signs of damage. The MFJ nylon was considerably cheaper and theoretically more durable. The black MFJ withstood force against the orchard canopy wire and cane imposed by the KHM torque limits, without any damage.

Observing video footage of LHR harvesting provided insight into the performance. When the end-effector enveloped a kiwifruit in a region of 'stiff' canopy, fruit would be successfully harvested without dropped and/or knocked fruit. This was generally the case regardless of clustering which endorses the cluster management classifier as part of the 'x-rank' algorithm and the non-intrusive design. However,

even in the ideal case of a non-compliant orchard canopy, fruit would still move from their original position throughout the harvesting phase due to the removal of neighorbouring fruit. This can be seen in the results for orchard region 2 where there were no drops across 50 fruit, but 20% of fruit were missed due to errors in fruit location as fruit moved. The main contributing factor in dropped fruit was the force applied to the canopy during the end-effector rotation. The LHR end-effectors rotation phase subject the canopy to observably more force than the KHM end-effector which was deterimental to performance. The majority of the canopy was fairly compliant and would shake to some degree, occasionally causing neighbouring fruit to drop. Compliant areas of canopy also amplified the effects of fruit knocking due to fruit being out of original position. In orchard region 5, an entire cluster of 5 fruit was dropped when harvesting an individual fruit due to a non-constrained branch connection being the weakest element across the load path produced by the end-effector force.

Other observations include fruit orientation and sub-phase time as a function of drop rate and harvestability. Kiwifruit tend to hang vertically; perpendicular to the ground plane. However, many fruit hang at some angle. This angle is not explicitly accounted for in the design of the LHR or KHM as the assumption is that the end-effector will approach the fruit from vertically beneath. This is likely responsible for some increase in drop rate or atleast some reduction in harvestability. A method of addressing this would be to implement a multiple DOF orientation kinematic structure such that the end-effector could approach the fruit along the fruit's stem axis regardless of hanging angle. Orientational degrees of freedom would also allow for a higher harvestability in that previously occluded fruit could be approached and harvested from a feasible direction. The sub-phase time was seen as a measure to reduce as part of the harvest cycle time, decreasing this time often results in an increase in velocity and acceleration of the end-effector as described in the optimization method used on the LHR. However, increasing speed is not necessarily conducive to increasing the amount of picked fruit. It was instead observed that drop rates were increased with reduced sub-phase time because of the amplified effect of fruit knocking and force subject to canopy during acceleration with fruit. This was observed during misc LHR testing and 2018 KHM harvesting. Accordingly, sub-phase acceleration and velocity may then be limited independent of kinematic structure due the potential for an increased drop rate. Further testing is needed to quantify these observations.

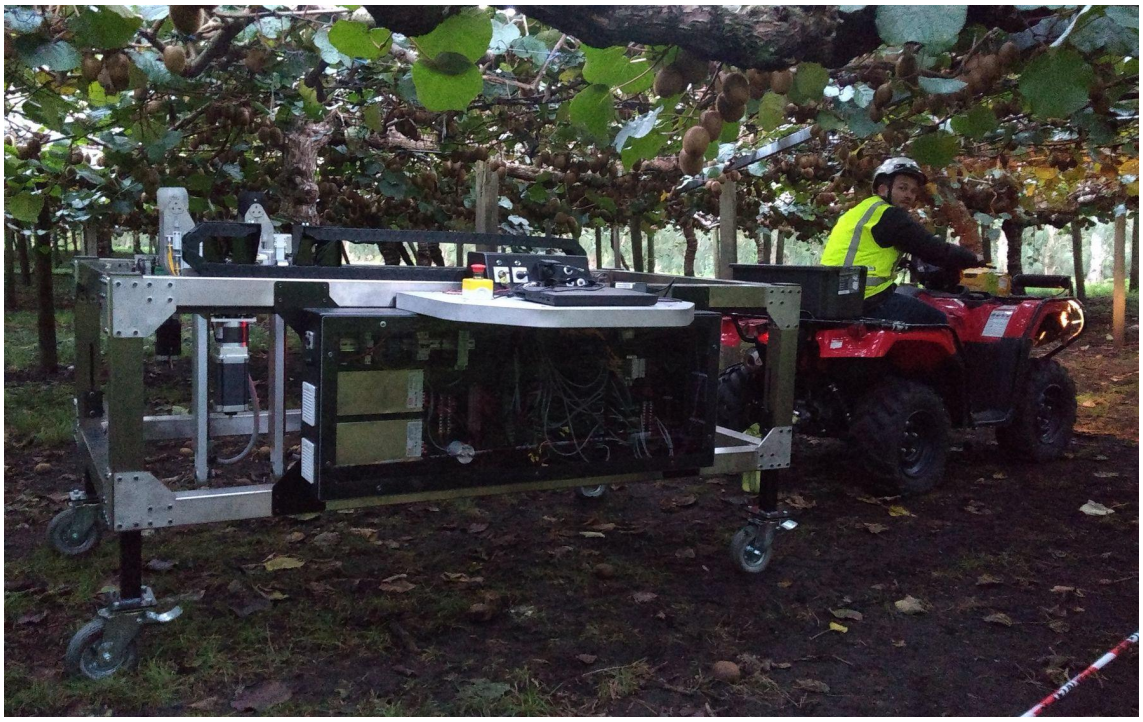

Figure 5.7: LHR towed through orchard with quadbike

Chapter 6

Conclusions

The objective for this study was to define important metrics for the robotic harvesting of kiwifruit and to propose a hardware configuration which could improve on the KHM. The initial hypothesis was that a prismatic axis robot may demonstrate improvement in multiple robot-arm cooperation by utilizing a shared work space along a common X-axis. After a review of relevant topics and systems, the research scope was focused on evaluating the following question:

Is a prismatic axis kinematic structure more effective than a rotational axis kinematic structure for the multiple-robot harvesting of kiwifruit?

KPI's were defined as evaluation and design measures. These included fruit damage, harvestability and nominal harvest cycle time. An equation specific to the KHM was derived for the latter which included measures of fruit per harvesting phase, time between fruit and a proposed work distribution constant W_D. The prismatic axis kinematic structure of the LHR allowed for an 88% greater work distribution constant W_D, a 40% greater harvestable taskspace volume V_h and 2.5 times greater overall workspace efficiency when compared to the KHM.

The harvest cycle time was defined by Eq. 3.2 and 3.4. The average volumetric density of fruit within the orchard taskspace can be derived from the average orchard having 10000 $\frac{trays}{hectare}$ and there being on average 33 $\frac{fruit}{tray}$ [67]. Thus, with a fruit-filled taskspace volume of approximately 3000 $\frac{m^3}{hectare}$ (with the assumption of a 300mm vertical span of fruit for any given phase), the average volumetric density of fruit is $\rho_v = 110\frac{fruit}{m^3}$. Williams et al. estimated the time taken to advance the phase with the AMMP and the time taken to identify and localizate kiwifruit as 3 seconds each. It was determined in Section 3.2 that direct sub-phase time comparisons are unreasonable due to different drive capacities and budgets. Section 5.1.2

alludes to a kinematically independent, sub-phase time limitation due to increased speed having a deterimental influence on drop rate. Thus, a reasonable assumption for a common sub-phase time would be $t_{sub-phase} = 2s$. Combining these variables the harvest cycle time is identical for the four-arm KHM and the two-arm LHR at $t = 1.18s$. When considering that the LHR and 'x-rank' algorithm was capable of maintaining a W_D value of 0.94 when operating both robot-arms in a fraction of workspace less than half of the LHR's total workspace. A reasonable assumption is that the LHR would maintain this 0.94 value with the same robot-arm density by instead doubling the amount of robot arms instead of halving the workspace. A four-arm LHR would achieve a harvest cycle time 80% greater than the four-arm KHM with $t = 0.66s$.

The LHR end-effector was developed to be non-intrusive to reduce fruit damage. It damaged 49% less fruit than the 2017 KHM end-effector. However, the 2018 version of the KHM damaged 26% less fruit than the LHR; this was predominantly down to the increased force subject to the canopy by the LHR. It was found that the 'x-rank' and 'greedy' registery algorithms were nearly identical in speed despite 'x-rank' having a 26% greater euclidean distance between sequentially registered fruit. The differential drive, rolling-element constrained design of the LHR was responsible for a significant increase in drive efficiency compared to a plain-bearing constrained design with motors not estranged from YZ motion.

There exists significant scope for improvement and further evaluation within this area of research. A preemtive driver behind the research is the prospect for commercialization, hence the broad-scope KPI's used as evaluation measures in this study. Arguably the most important KPI is fruit damage from the dropping and knocking of fruit during harvesting. As mentioned in Section 3.2.1, the damaging of fruit directly affects the orchard owners profit margin from lost revenue. Therefore, a robotic system which damages more fruit than a human team of skilled pickers would need to offset the cost of lost revenue as well as hourly rate and operational overheads in order to be commercially competitive. In addition, an increase in damaged fruit would require a greater orchard area to achieve the same export volumes. A potentially feasible business model might be that a future KHM/LHR picks ∼60% of all kiwifruit in an orchard but maintains a damage rate comparable to that of human pickers.

Some of the main barriers to reducing the drop/knock rate are in the end-effector detachment method, the localization error of machine vision, orientation and size variance of fruit, and the fact that kiwifruit themselves move out of their

original location. One of the limitations to this study is that the harvest cycle time equation derived for the KHM/LHR does not factor in any additional downtimes due to in-phase identification and localization as fruit move out of original position. Williams et al. makes mention of this as a limiting factor. One potential solution to address one of these barriers, mentioned in section 5.1.2, is to use some kinematic orientation structure of the end-effector to adapt to fruit of different orientation. This would also improve the harvestability of fruit by providing different approach angles to previously occluded fruit. Another potential solution would be the use of a visual-servo system [68] such as commonly used in citrus harvesting [69] to reduce localization error and dynamically follow fruit positions without the need for additional downtime. A visual-servo system would likely reduce the sub-phase time but this may also be beneficial to preventing fruit damage. There is likely to a be a trade-off in feasibility for each of these prospective solutions; further study would need to be done to quantify this.

In summary, this study has found that a prismatic axis kinematic structure is more effective than a rotational axis kinematic structure for the multiple-robot harvesting of kiwifruit with fixed end-effector orientation. Robotic kiwifruit harvesting systems of the future may benefit from and/or require an orientation structure of the end-effector to reduce fruit damage and increase harvestability. Further study would need to be done into comparitive manipulability measures (Section 2.1), scheduling methods and the effects on work distribution to establish whether a prismatic axis structure remains favourable.

6.1 Future Work

The outcome of this study likely warrants the continued development into a successive iteration of the LHR with a larger budget and a minimum of four robot-arms. It is predicted that current studies in crop estimation may aid in the development of a design brief for this system such as providing a more detailed understanding of the orchard taskspace. This includes a better measure of fruit height variance, quantifying heterogenity of fruit distribution and fruit orientation.

A successive LHR would benefit from collision prevention software and would likely have a minimally optimized robot-arm width, servo-driven motion (as opposed to stepper motors) and potentially an orientation structure for adding DOF's to the manipulation. A visual servo approach to machine vision would likely minimize spatial error whilst allowing dexterous path planning at the cost of speed.

The current approach has been to use a multi-purpose platform to provide autonomous motion to the KHM. It may be worth revising this approach towards the development of an optimized kiwifruit harvesting robotic system built for that single task.

Bibliography

[1] S. Patel and T. Sobh, "Manipulator Performance Measures - A Comprehensive Literature Survey," *Journal of Intelligent & Robotic Systems*, vol. 77, pp. 547–570, mar 2015.

[2] T. Tanev and B. Stoyanov, "On the Performance Indexes for Robot Manipulators," *Problems of engineering cybernetics and robotics*, 2000.

[3] G. M. Cloutier, A. Jutard, and M. Bétemps, "A robot-task conformance index for the design of robotized cells," *Robotics and Autonomous Systems*, vol. 13, pp. 233–243, dec 1994.

[4] B. Zion, M. Mann, D. Levin, A. Shilo, D. Rubinstein, and I. Shmulevich, "Harvest-order planning for a multiarm robotic harvester," *Computers and Electronics in Agriculture*, vol. 103, pp. 75–81, apr 2014.

[5] "AGROBOT - Strawberries Harvester, http://agrobot.com, 2018,"

[6] A. J. Scarfe, *Development of an autonomous kiwifruit harvester*. PhD thesis, Massey University, 2012.

[7] Grandview Research, "Precision Farming/Agriculture Market Size, Share — Industry Report 2025," tech. rep., 2018.

[8] "Key Findings and Advance Tables," *World Population Prospects: The 2017 Revision*, 2017.

[9] "Key Facts," *World Urbanization Prospects: The 2018 Revision*, p. 2.

[10] E. Boserup, *The Conditions of Agricultural Growth*. Routledge, jun 2005.

[11] A. McBratney, B. Whelan, T. Ancev, and J. Bouma, "Future Directions of Precision Agriculture," *Precision Agriculture*, vol. 6, pp. 7–23, feb 2005.

[12] F. A. Auat Cheein and R. Carelli, "Agricultural Robotics: Unmanned Robotic Service Units in Agricultural Tasks," *IEEE Industrial Electronics Magazine*, vol. 7, pp. 48–58, sep 2013.

[13] T. Burks, F. Villegas, M. Hannan, S. Flood, B. Sivaraman, V. Subramanian, and J. Sikes, "Engineering and horticultural aspects of robotic fruit harvesting: Opportunities and constraints," *HortTechnology*, vol. 15, no. 1, pp. 79–87, 2005.

[14] K. R. Everett, R. K. Taylor, M. K. Romberg, J. Rees-George, R. A. Fullerton, J. L. Vanneste, and M. A. Manning, "First report of Pseudomonas syringae pv. actinidiae causing kiwifruit bacterial canker in New Zealand," *Australasian Plant Disease Notes*, vol. 6, pp. 67–71, dec 2011.

[15] "Zespri 5 YEAR OUTLOOK," tech. rep., 2017.

[16] A. J. Scarfe, R. C. Flemmer, H. H. Bakker, and C. L. Flemmer, "Development of an autonomous kiwifruit picking robot," *ICARA 2009 - Proceedings of the 4th International Conference on Autonomous Robots and Agents*, pp. 380–384, 2009.

[17] K. J. Waldron and J. Schmiedeler, "Kinematics," in *Springer Handbook of Robotics*, pp. 11–36, Cham: Springer International Publishing, 2016.

[18] Z.-C. Lia and C.-H. Menq, "The dexterous workspace of simple manipulators," *IEEE Journal on Robotics and Automation*, vol. 4, no. 1, pp. 99–103, 1988.

[19] R. Vijaykumar, K. Waldron, and M. Tsai, "Geometric Optimization of Serial Chain Manipulator Structures for Working Volume and Dexterity," *The International Journal of Robotics Research*, vol. 5, pp. 91–103, jun 1986.

[20] A. Kumar and K. J. Waldron, "The Workspaces of a Mechanical Manipulator," *Journal of Mechanical Design*, vol. 103, no. 3, p. 665, 1981.

[21] J. K. Salisbury and J. J. Craig, "Articulated Hands," *The International Journal of Robotics Research*, vol. 1, pp. 4–17, mar 1982.

[22] Jin-Oh Kim and K. Khosla, "Dexterity measures for design and control of manipulators," in *Proceedings IROS '91:IEEE/RSJ International Workshop on Intelligent Robots and Systems '91*, pp. 758–763, IEEE, 1991.

[23] T. Yoshikawa, "Manipulability of Robotic Mechanisms," *The International Journal of Robotics Research*, 1985.

[24] K. C. Olds, "Global Indices for Kinematic and Force Transmission Performance in Parallel Robots," *IEEE Transactions on Robotics*, vol. 31, pp. 494–500, apr 2015.

[25] S. L. Chiu, "Task Compatibility of Manipulator Postures," *The International Journal of Robotics Research*, vol. 7, pp. 13–21, oct 1988.

[26] S. Lee, "Dual redundant arm configuration optimization with task-oriented dual arm manipulability," *IEEE Transactions on Robotics and Automation*, vol. 5, no. 1, pp. 78–97, 1989.

[27] F. Park and Jin Wook Kim, "Manipulability and singularity analysis of multiple robot systems: a geometric approach," in *Proceedings. 1998 IEEE International Conference on Robotics and Automation (Cat. No.98CH36146)*, vol. 2, pp. 1032–1037, IEEE.

[28] D. P. Garg and M. Kumar, "Optimization techniques applied to multiple manipulators for path planning and torque minimization," *Engineering Applications of Artificial Intelligence*, vol. 15, pp. 241–252, jun 2002.

[29] N. M. F. Ferreira and J. A. T. Machado, "Manipulability Analysis of Two-Arm Robotic Systems," 2018.

[30] V. Scheinman, J. M. McCarthy, and J.-B. Song, "Mechanism and Actuation," in *Springer Handbook of Robotics*, pp. 67–90, Cham: Springer International Publishing, 2016.

[31] P. Sanchez-Sanchez and F. Reyes-Cortes, "Cartesian Control for Robot Manipulators," in *Robot Manipulators Trends and Development*, InTech, mar 2010.

[32] K. Sanders, "Orange Harvesting Systems Review," *Biosystems Engineering*, vol. 90, pp. 115–125, feb 1968.

[33] S. Bachche, "Deliberation on Design Strategies of Automatic Harvesting Systems: A Survey," *Robotics*, vol. 4, no. 2, p. 194, 2015.

[34] C. W. Bac, E. J. van Henten, J. Hemming, and Y. Edan, "Harvesting Robots for High-value Crops: State-of-the-art Review and Challenges Ahead," *Journal of Field Robotics*, vol. 31, pp. 888–911, nov 2014.

[35] Y. Sarig, "Robotics of Fruit Harvesting: A State-of-the-art Review," *Journal of Agricultural Engineering Research*, vol. 54, pp. 265–280, apr 1993.

[36] P. Li, S.-h. Lee, and H.-Y. Hsu, "Review on fruit harvesting method for potential use of automatic fruit harvesting systems," *Procedia Engineering*, vol. 23, pp. 351–366, 2011.

[37] K. Kapach, E. Barnea, R. Mairon, Y. Edan, and O. B. Shahar, "Computer vision for fruit harvesting robots – state of the art and challenges ahead," *International Journal of Computational Vision and Robotics*, vol. 3, no. 1/2, p. 4, 2012.

[38] E. J. V. Henten, D. A. Van 't Slot, C. W. J. Hol, and L. G. Van Willigenburg, "Optimal manipulator design for a cucumber harvesting robot,"

[39] G. Carbone, E. Ottaviano, and M. Ceccarelli, "An optimum design procedure for both serial and parallel manipulators," *Proceedings of the Institution of Mechanical Engineers, Part C: Journal of Mechanical Engineering Science*, vol. 221, pp. 829–843, jul 2007.

[40] S. Han, S. Xueyan, Z. Tiezhong, Z. Bin, and X. Liming, "Design optimisation and simulation of structure parameters of an eggplant picking robot," *New Zealand Journal of Agricultural Research*, vol. 50, pp. 959–964, dec 2007.

[41] J. T. Baur, *Agricultural Manipulators Simulation, Design and Motion Planning.* PhD thesis, 2014.

[42] J. Baur, J. Pfaff, H. Ulbrich, and T. Villgrattner, "Design and development of a redundant modular multipurpose agricultural manipulator," in *2012 IEEE/ASME International Conference on Advanced Intelligent Mechatronics (AIM)*, pp. 823–830, IEEE, jul 2012.

[43] V. Bloch, A. Degani, and A. Bechar, "A methodology of orchard architecture design for an optimal harvesting robot," *Biosystems Engineering*, vol. 166, pp. 126–137, feb 2018.

[44] E. van Henten, J. Hemming, B. van Tuijl, J. Kornet, J. Meuleman, J. Bontsema, and E. van Os, "An Autonomous Robot for Harvesting Cucumbers in Greenhouses," *Autonomous Robots*, vol. 13, no. 3, pp. 241–258, 2002.

[45] C. W. Bac, J. Hemming, B. van Tuijl, R. Barth, E. Wais, and E. J. van Henten, "Performance Evaluation of a Harvesting Robot for Sweet Pepper," *Journal of Field Robotics*, vol. 34, pp. 1123–1139, sep 2017.

[46] M. M. Foglia and G. Reina, "Agricultural Robot for Radicchio Harvesting," *Journal of Field Robotics*, vol. 23, no. 67, pp. 363–377, 2006.

[47] W. Lili, Z. Bo, F. Jinwei, H. Xiaoan, W. Shu, L. Yashuo, Q. Zhou, and W. Chongfeng, "Development of a tomato harvesting robot used in greenhouse," *International Journal of Agricultural and Biological Engineering*, vol. 10, pp. 140–149, jul 2017.

[48] S. Hayashi, S. Yamamoto, S. Saito, Y. Ochiai, J. Kamata, M. Kurita, and K. Yamamoto, "Field Operation of a Movable Strawberry-harvesting Robot using a Travel Platform," *JARQ*, vol. 48, no. 3, pp. 307–316, 2014.

[49] A. Silwal, J. Davidson, M. Karkee, C. Mo, J. R. Davidson, Q. Zhang, and K. Lewis, "Design, integration, and field evaluation of a robotic apple harvester,"

[50] J. J. Roldán, J. del Cerro, D. Garzón-Ramos, P. Garcia-Aunon, M. Garzón, J. de León, and A. Barrientos, "Robots in Agriculture: State of Art and Practical Experiences," in *Service Robots*, InTech, jan 2018.

[51] O. Maimon, "The robot task-sequencing planning problem," *IEEE Transactions on Robotics and Automation*, vol. 6, no. 6, pp. 760–765, 1990.

[52] R. Roy Harrell, "Economic Analysis of Robotic Citrus Harvesting in Florida," *Transactions of the ASAE*, vol. 30, no. 2, pp. 0298–0304, 1987.

[53] M. Recce, J. Taylor, A. Plebe, and G. Tropiano, "Vision and neural control for an orange harvesting robot,"

[54] Y. Edan, B. A. Engel, and G. E. Miles, "Intelligent control system simulation of an agricultural robot," *Journal of Intelligent & Robotic Systems*, vol. 8, pp. 267–284, oct 1993.

[55] "No Title,"

[56] M. P. Mann, D. Rubinstein, I. Shmulevich, R. Linker, and B. Zion, "Motion Planning of a Mobile Cartesian Manipulator for Optimal Harvesting of 2-D Crops," *Transactions of the ASABE*, vol. 57, pp. 283–295, mar 2014.

[57] M. P. Mann, B. Zion, I. Shmulevich, D. Rubinstein, and R. Linker, "Combinatorial Optimization and Performance Analysis of a Multi-arm Cartesian Robotic Fruit Harvester—Extensions of Graph Coloring," *Journal of Intelligent & Robotic Systems*, vol. 82, pp. 399–411, jun 2016.

[58] "Harvest Croo, http://www.harvestcroorobotics.com, 2018."

[59] H. Williams, M. H. Jones, M. Nejati, J. Bell, N. Penhall, H. A. Seok, J. Lim, B. MacDonald, M. Seabright, J. Barnett, M. Duke, and A. Scarfe, "Robotic Kiwifruit Harvesting using Machine Vision, Convolutional Neural Networks, and Robotic Arms," *Biosystems Engineering*, p. To be published, 2017.

[60] W. P. Snelgar, G. Hopkirk, R. J. Seelye, P. J. Martin, and P. J. Manson, "Relationship between canopy density and fruit quality of kiwifruit," *New Zealand Journal of Crop and Horticultural Science*, vol. 26, pp. 223–232, 1998.

[61] "Part 1: Tolerances of Linear and angular dimensions without individual tolerance indications (ISO 2768-1:1989(en))," in *ISO 2768: General Tolerances*, ch. 1, 1989.

[62] Jones Douglas, "Stepping Motor Physics," in *Stepping motors*, ch. 2, The University of Iowa, Department of Computer Science, 1995.

[63] T. J. Ypma, "Historical Development of the Newton–Raphson Method," *SIAM Review*, vol. 37, pp. 531–551, dec 1995.

[64] J. C. Lagarias, J. A. Reeds, M. H. Wright, and P. E. Wright, "Convergence Properties of the Nelder–Mead Simplex Method in Low Dimensions," *SIAM Journal on Optimization*, vol. 9, pp. 112–147, jan 1998.

[65] D. S. Johnson and L. A. Mcgeoch, "The Traveling Salesman Problem: A Case Study in Local Optimization," 1995.

[66] K. D. Nguyen, T.-C. Ng, and I.-M. Chen, "On Algorithms for Planning S-Curve Motion Profiles," *International Journal of Advanced Robotic Systems*, vol. 5, p. 11, mar 2008.

[67] N. Plant and Food Research, "Fresh Facts 2016 - New Zealand horticulture-reaching new highs." 2016.

[68] P. I. Corke, "Visual control of robot manipulators - a review," tech. rep., 1994.

[69] M. Hannan and T. Burks, "Current Developments in Automated Citrus Harvesting," in *ASAE/CSAE Annual International Meeting*, (Ottawa, Canada), 2004.